Modulation of biophysical properties of nucleocapsid protein in the mutant spectrum of SARS-CoV-2

Ai Nguyen[1], Huaying Zhao[1], Dulguun Myagmarsuren[1], Sanjana Srinivasan[1], Di Wu[2], Jiji Chen[3], Grzegorz Piszczek[2], Peter Schuck[1]*

[1]Laboratory of Dynamics of Macromolecular Assembly, National Institute of Biomedical Imaging and Bioengineering, National Institutes of Health, Bethesda, United States; [2]Biophysics Core Facility, National Heart, Lung, and Blood Institute, National Institutes of Health, Bethesda, United States; [3]Advanced Imaging and Microscopy Resource, National Institute of Biomedical Imaging and Bioengineering, National Institutes of Health, Bethesda, United States

*For correspondence:
schuckp@mail.nih.gov

Abstract Genetic diversity is a hallmark of RNA viruses and the basis for their evolutionary success. Taking advantage of the uniquely large genomic database of SARS-CoV-2, we examine the impact of mutations across the spectrum of viable amino acid sequences on the biophysical phenotypes of the highly expressed and multifunctional nucleocapsid protein. We find variation in the physicochemical parameters of its extended intrinsically disordered regions (IDRs) sufficient to allow local plasticity, but also observe functional constraints that similarly occur in related coronaviruses. In biophysical experiments with several N-protein species carrying mutations associated with major variants, we find that point mutations in the IDRs can have nonlocal impact and modulate thermodynamic stability, secondary structure, protein oligomeric state, particle formation, and liquid-liquid phase separation. In the Omicron variant, distant mutations in different IDRs have compensatory effects in shifting a delicate balance of interactions controlling protein assembly properties, and include the creation of a new protein-protein interaction interface in the N-terminal IDR through the defining P13L mutation. A picture emerges where genetic diversity is accompanied by significant variation in biophysical characteristics of functional N-protein species, in particular in the IDRs.

eLife assessment

This **important** manuscript provides new insights into the biophysics of the SARS-CoV-2 nucleocapsid. The evidence, which relies on a **convincing** combination of genetic and biophysical data, nicely supports the conclusions.

Introduction

A salient characteristic of RNA viruses is their high error rate in transcription and their resulting quasi-species nature (*Eigen, 1996*; *Domingo and Holland, 1997*). This diversity is also reflected in the ensemble of consensus sequences sampled across the infected host population, as is apparent in the GISAID (Global Initiative on Sharing All Influenza Data) repository of SARS-CoV-2 genomes (*Elbe and Buckland-Merrett, 2017*). With currently ≈15 million entries, this unprecedented large database has provided the basis for phylogenetic analyses that have identified critical amino acid mutations associated with immune evasion, infectivity, and disease severity, and allowed the rapid identification of variants of concern (*Greaney et al., 2022*; *Kepler et al., 2021*; *Obermeyer et al., 2022*; *Rochman*

eLife digest Like other types of RNA viruses, the genetic material of SARS-CoV-2 (the agent responsible for COVID-19) is formed of an RNA molecule which is prone to accumulating mutations. This gives SARS-CoV-2 the ability to evolve quickly, and often to remain one step ahead of treatments. Understanding how these mutations shape the behavior of RNA viruses is therefore crucial to keep diseases such as COVID-19 under control.

The gene that codes for the protein that 'packages' the genetic information inside SARS-CoV-2 is particularly prone to mutations. This nucleocapsid (N) protein participates in many key processes during the life cycle of the virus, including potentially interfering with the immune response. Exactly how the physical properties of the N-Protein are impacted by the mutations in its genetic sequence remains unclear.

To investigate this question, Nguyen et al. predicted the various biophysical properties of different regions of the N-protein based on a computer-based analysis of SARS-CoV-2 genetic databases. This allowed them to determine if specific protein regions were positively or negatively charged in different mutants. The analyses showed that some domains exhibited great variability in their charge between protein variants – reflecting the fact that the corresponding genetic sequences showed high levels of plasticity. Other regions remained conserved, however, including across related coronaviruses.

Nguyen et al. also conducted biochemical experiments on a range of N-proteins obtained from clinically relevant SARS-CoV-2 variants. Their results highlighted the importance of protein segments with no fixed three-dimensional structure. Mutations in the related sequences created high levels of variation in the physical properties of these 'intrinsically disordered' regions, which had wide-ranging consequences. Some of these genetic changes even gave individual N-proteins the ability to interact with each other in a completely new way.

These results shed new light on the relationship between genetic mutations and the variable physical properties of RNA virus proteins. Nguyen et al. hope that this knowledge will eventually help to develop more effective treatments for viral infections.

et al., 2021; *Viana et al., 2022*). The vast majority of mutations, however, seem inconsequential in that they usually do not lead to any fixed substitutions. Nonetheless, the mutant spectrum exhaustively describes a landscape of amino acids that may occupy any position in the viral proteins, as in a natural deep mutational scan (*Bloom and Neher, 2023*; *Schuck and Zhao, 2023*; *Zhao et al., 2022*). Biophysical constraints implicit in the shape of such landscapes are key to understand the function and molecular evolution of viral proteins (*Starr and Thornton, 2016*; *Wang et al., 2021*).

Unfortunately, the wealth of genomic information on SARS-CoV-2 stands in stark contrast with our knowledge of the phenotypic consequences of sequence mutations. In conjunction with biophysical and structural studies, inspections of local mutations have increased our understanding of mechanisms of SARS-CoV-2 entry, mechanisms of replication and assembly, and interaction with various host factors (*Dadonaite et al., 2023*; *Del Veliz et al., 2021*; *Greaney et al., 2022*; *Hu et al., 2023*; *Stevens et al., 2022*; *Syed et al., 2021*; *Zhao et al., 2023*; *Zhao et al., 2022*). Furthermore, the range of naturally occurring mutations at target sites is an important consideration for potential drugs, vaccines, and diagnostics (*Artesi et al., 2020*; *Saldivar-Espinoza et al., 2022*; *Tian et al., 2022*). Outside these focused studies of relatively well-understood hot spots, however, the mutational landscape has remained relatively unexplored.

Biophysical fitness landscapes have been studied with regard to observables such as thermal stability of globular proteins, solvent accessibility, catalytic activity, or binding affinity of protein-protein interfaces, which has led to significant advances in understanding relationship between molecular properties, population fitness, and evolutionary processes (*Bershtein et al., 2017*; *Bloom et al., 2006*; *Echave and Wilke, 2017*; *Lässig et al., 2017*; *Liberles et al., 2012*; *Serohijos and Shakhnovich, 2014*; *Sikosek and Chan, 2014*; *Wang et al., 2015*). However, it was found that constraints for evolution of intrinsically disordered regions (IDRs) are much different from those of globular proteins (*Brown et al., 2010*; *Lafforgue et al., 2022*). Generally, intrinsic disorder and loose packing is a common characteristic of many RNA virus proteins (*Tokuriki et al., 2009*), which is thought to promote functional promiscuity, permit greater diversity, and enhance evolvability to adopt new functions with
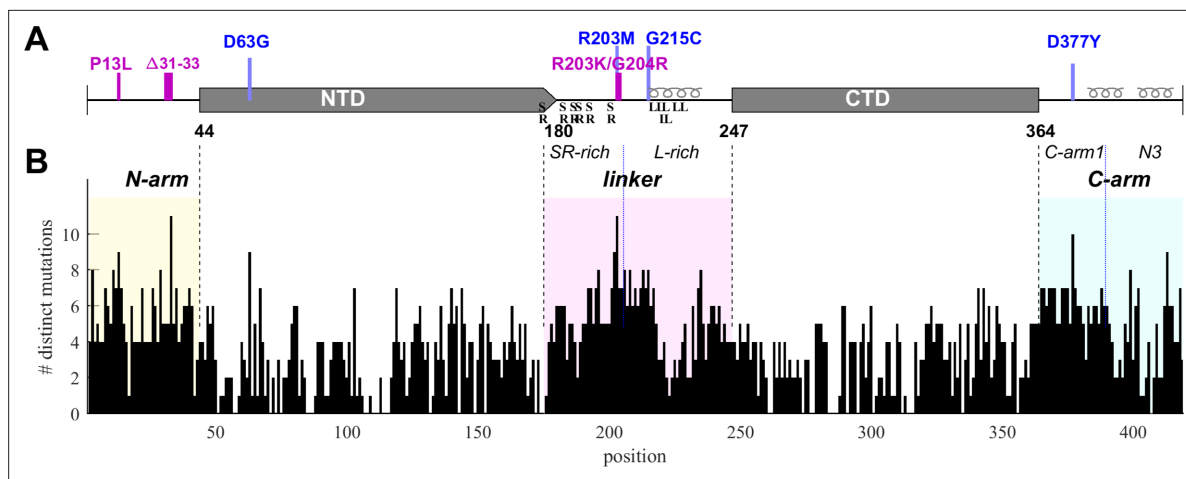
Figure 1. Structural organization and sequence plasticity of N-protein. (**A**) Schematics of folded regions (NTD and CTD, rectangles) and disordered regions (N-arm, linker, and C-arm, straight line) along the N-protein sequence. Defining mutations from the Delta variant are indicated in blue, those from Omicron variants in magenta. Transient helices in the disordered regions are highlighted, as well as SR-rich and L-rich linker sequences and the C-terminal N3 region. (**B**) Histogram of the number of distinct amino acid mutations at each position. For clarity and reference to other figures, intrinsically disordered regions (IDRs) are shaded with N-arm highlighted in yellow, linker in magenta, and C-arm in cyan.

few mutations (*Charon et al., 2018*; *Gitlin et al., 2014*; *Tokuriki and Tawfik, 2009*). One possible mechanism is viral mimicry of host-protein short linear motifs (SLiMs) that allow binding to host protein domains and cause subversion of host cellular pathways (*Davey et al., 2015*; *Davey et al., 2011*; *Hagai et al., 2014*; *Kruse et al., 2021*; *Mihalič et al., 2023*; *Schuck and Zhao, 2023*; *Shuler and Hagai, 2022*). It was also shown how nonlocal biophysical properties, such as the charge of IDRs, can be relevant evolutionary traits (*Zarin et al., 2021*; *Zarin et al., 2017*). More recently, it was recognized that the formation of membrane-less cellular compartments driven by liquid-liquid phase separation (LLPS) is a key aspect of many intrinsically disordered proteins, including many viral proteins (*Cascarina and Ross, 2022*; *Zhang et al., 2023*). What kind of sequence constraints may derive from the biophysical requirement to conserve LLPS properties is currently only emerging (*Brown et al., 2011*; *Chin et al., 2022*; *Ho and Huang, 2022*; *Lin et al., 2017*; *Riback et al., 2017*).

The goal of the present work is to probe the phenotypic diversity with respect to several biophysical properties of SARS-CoV-2 nucleocapsid (N-)protein, taking advantage of the vast mutational landscape of SARS-CoV-2. N-protein is the most abundant viral protein in the infected cell (*Finkel et al., 2021*), and as we reported previously (*Zhao et al., 2022*), it is also the most diverse structural protein with approximately 86% of its 419 residues capable of assuming on average four to five different amino acids evidently without impairment of viability. The highest frequency of mutations occurs in the substantial IDRs which are the N-arm, linker, and C-arm that flank and connect the folded nucleic acid binding domain (NTD) and the dimerization domain (CTD) (*Figure 1*). The IDRs comprise approximately half of the molecule and allow large conformational fluctuations (*Botova et al., 2024*; *Cubuk et al., 2021*; *Redzic et al., 2021*). The eponymous structural function of N-protein is that of scaffolding genomic RNA for virion assembly. It proceeds via nucleic acid (NA) binding-induced conformational changes and oligomerization, leading to the formation of ribonucleoprotein (RNP) particles with as-of-yet unknown molecular architecture, ≈38 of which are arranged like beads-on-a-string in the viral particle (*Carlson et al., 2022*; *Cubuk et al., 2021*; *Klein et al., 2020*; *Yao et al., 2020*; *Zhao et al., 2024*; *Zhao et al., 2023*; *Zhao et al., 2021*), and are anchored through binding of N-protein to viral M-protein (*Lu et al., 2021*; *Masters, 2019*). Beyond this structural role, N-protein is highly multifunctional and binds to multiple host proteins to modulate or exploit different pathways, including stress granules (*Biswal et al., 2022*; *Gordon et al., 2020*; *Savastano et al., 2020*), the type 1 interferon signaling pathway (*Chen et al., 2020*; *Li et al., 2020*), the NLRP3 inflammasome (*Pan et al., 2021*), and others, as recently reviewed (*Wu et al., 2023*; *Yu et al., 2023*). N-protein can form macromolecular condensates through LLPS that aid in assembly functions and interactions with host proteins (*Carlson et al., 2020*; *Cascarina and Ross, 2022*; *Cubuk et al., 2021*; *Iserman et al., 2020*; *Jack et al., 2021*; *Lu et al., 2021*; *Perdikari et al., 2020*; *Savastano et al., 2020*). In addition, it is

also localized at exterior cell surfaces, where it was found to bind many different chemokines, likely manipulating innate immunity through chemokine sequestration (*López-Muñoz et al., 2022*).

The large number of structural and non-structural N-protein functions poses the question of how they are conserved in light of the significant sequence diversity. In the present work we computationally evaluate the range of several biophysical traits resulting from diversity in the SARS-CoV-2 N-protein folded domains and IDRs across the observed mutant spectrum, as well as related coronaviruses. In complementary biophysical experiments with several representative N-protein mutants derived from SARS-CoV-2 variants of concern, we characterize their variation in thermodynamic stability, secondary structure, oligomeric state, energetics of NA binding, assembly, and LLPS propensity. We find that a large biophysical parameter space is available for viable N-protein, with the potential for mutations to exert nonlocal effects modulating overall protein biophysical properties.

Results

Distribution of physicochemical properties across the SARS-CoV-2 mutant spectrum

SARS-CoV-2 sequence data were downloaded from Nextstrain (*Hadfield et al., 2018*) in January 2023 and 5.06 million high-quality sequences were selected for analysis. The N-protein amino acid sequences exhibit ≈43 million instances of mutations distributed across ≈92% of its residues. We have previously characterized this dataset with regard to the amino acid mutational landscape of N-protein, and found mutation frequencies that are strongly dependent on position and largely time-invariant, except for the defining mutations arising in variants of concern, the latter comprising ≈36% Delta variant and ≈49% Omicron variant sequences (*Schuck and Zhao, 2023*). A histogram of the number of different amino acids mutations that are found at each residue is shown in *Figure 1B*. It may be discerned that sequence plasticity is highest in the IDRs, with an average of 5.2 different possible amino acid mutations at each residue compared to 2.9 different mutations on average in the folded domains.

Exploiting the N-protein mutational landscape and sequence data, previous work in our laboratory has focused on local amino acid sequence properties such as mutation effects on transient structural features in the linker IDR (*Zhao et al., 2023*) and the creation of SLiMs (*Schuck and Zhao, 2023*). However, nonlocal biophysical properties may also be functionally critical and evolutionarily conserved despite amino acid sequence heterogeneity in IDRs (*Zarin et al., 2021*; *Zarin et al., 2017*). The sequence ensembles extracted from the genomic database allow us to ask whether physicochemical properties are constrained or can vary across viable sequences of the mutation spectrum.

To this end, genome data were sorted into unique groups with distinct N-protein amino acid sequences, each sequence carrying a set of distinct mutations that represent a viable N-protein species. For a robust analysis, each mutated sequence was required to be represented in at least 10 different genomes in the database. This led to 6300 distinct full-length N-protein sequences (N-FL; 1–419). We similarly subdivided the N-protein into different regions (*Figure 1A*) and grouped unique sets of mutations in each region: For the folded domains we found 720 distinct NTD (N:45–179) and 399 distinct CTD (N:248–363) sequences, while for the IDRs there are 512 N-arm (N:1–44), 1039 linker (N:175–247), and 556 C-arm (N:364–419) sequences. (Due to ambiguity in delineation between NTD and linker, designations overlapping in 175–180 were used to avoid artificial truncation and permit conservative evaluation of the properties of each domain.) Further subdividing the linker there are 349 distinct sequences for the SR-rich region (N:175–205) and 442 for the L-rich region (N:206–247), respectively. Finally, similarly subdividing the C-arm we obtained the 176 sequences for the N3 region (N:390–419) and 242 for the remainder of the C-arm (N:364–389).

We first examine polarity and hydrophobicity of N-protein and different regions based on their amino acid compositions. As shown in beehive plots of *Figure 2*, where each of the partially overlapping black dots represents one species from the cloud of mutant sequences, the index values of all N-FL sequences fall within a very narrow range (left column). Properties of the full-length protein may obscure significant differences on a smaller scale, in particular since the polarity and hydrophobicity indices are weighted-average properties. Focusing on folded N-protein modules, we find that hydrophobicity is uniformly high and polarity correspondingly low in the folded NTD and CTD domains, which is consistent with the expectation that folded structures are stabilized by buried hydrophobic
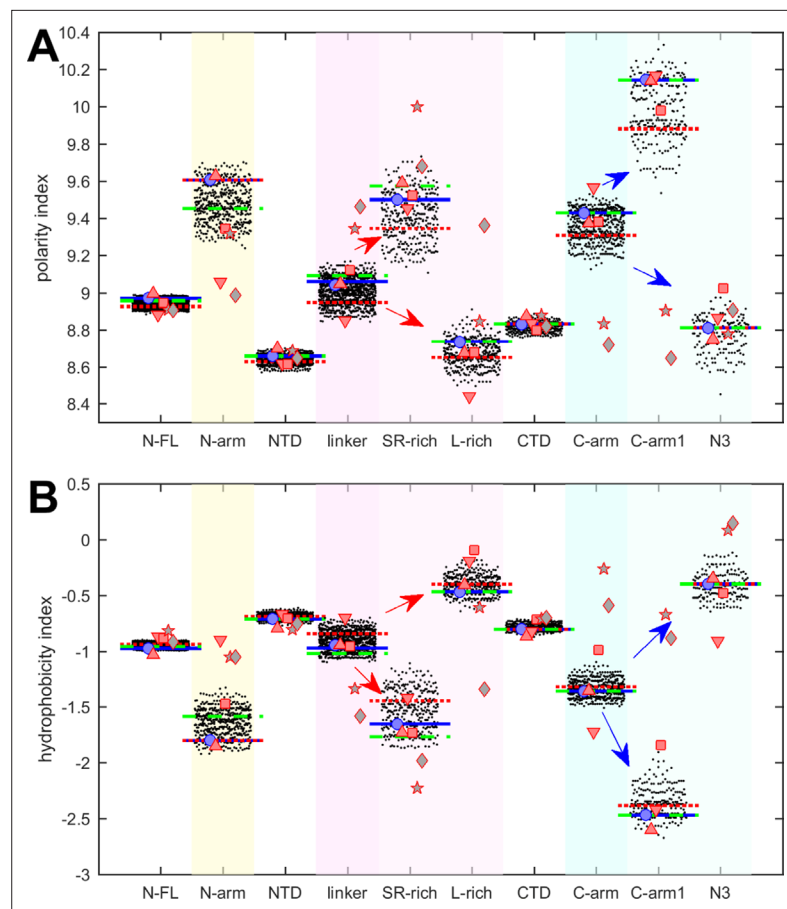
Figure 2. Beehive plots showing the distributions of polarity and hydrophobicity of viable N-protein species across the mutant spectrum. The polarity index (**A**) and hydrophobicity index (**B**) was calculated based on amino acid composition for all distinct sequences of N-FL, the folded domains (NTD and CTD), and the intrinsically disordered regions (IDRs) (N-arm, linker, and C-arm). Further subdivisions of the linker into the SR-rich and L-rich regions, and subdivisions of the C-arm into the N3 region and the C-terminal remainder of the C-arm (C-arm1) are indicated in the arrows. Highlighted by horizontal lines are the values for the corresponding peptides from the ancestral sequence Wuhan-Hu-1 (blue), and including the defining mutations of the Delta variant (dotted red) and the Omicron variant (dashed green), respectively. Symbols indicate values for SARS-CoV-2 (ancestral reference, light blue circles), and corresponding peptides from SARS-CoV-1 (red up triangles), Middle East respiratory syndrome coronavirus (MERS) (red down triangles), murine hepatitis virus (MHV) (red squares), human coronavirus NL63 (gray pentagrams), and the bat coronavirus APD51511.1 (gray diamonds).

residues (*Eisenberg and McLachlan, 1986*; *Kauzmann, 1959*). By contrast, IDRs exhibit significantly higher polarity and lower hydrophobicity. In particular, the N-arm and C-arm are most polar: despite a very large dispersion across the mutant spectrum, their values do not overlap with those of the folded domains.

It is useful to subdivide the linker IDR further to distinguish the SR-rich region (N:175–205), which exhibits high polarity and low hydrophobicity, from the L-rich region (N:206–247), which exhibits opposite behavior and is among the sequence stretches with lowest polarity values and highest hydrophobicity (*Figure 2*, red arrows in magenta shaded columns). Despite significant spread across the mutant spectrum, there is no overlap in these properties, which suggests biophysical constraints require the distinct polar and non-polar properties of the SR-rich region and the L-rich region, respectively. Indeed, these regions in the linker IDR have been recognized to play distinct functional roles: The SR-rich region provides a major hub for phosphorylation, aids in NA binding, and mediates NA binding-induced allosteric interactions between NTD and the L-rich region (*Pontoriero et al., 2022*; *Yaron et al., 2022*; *Zhao et al., 2023*). This is distinct from the L-rich region, which has a propensity for the formation of transient helices that interact with NSP3 (*Bessa et al., 2022*), and can assemble
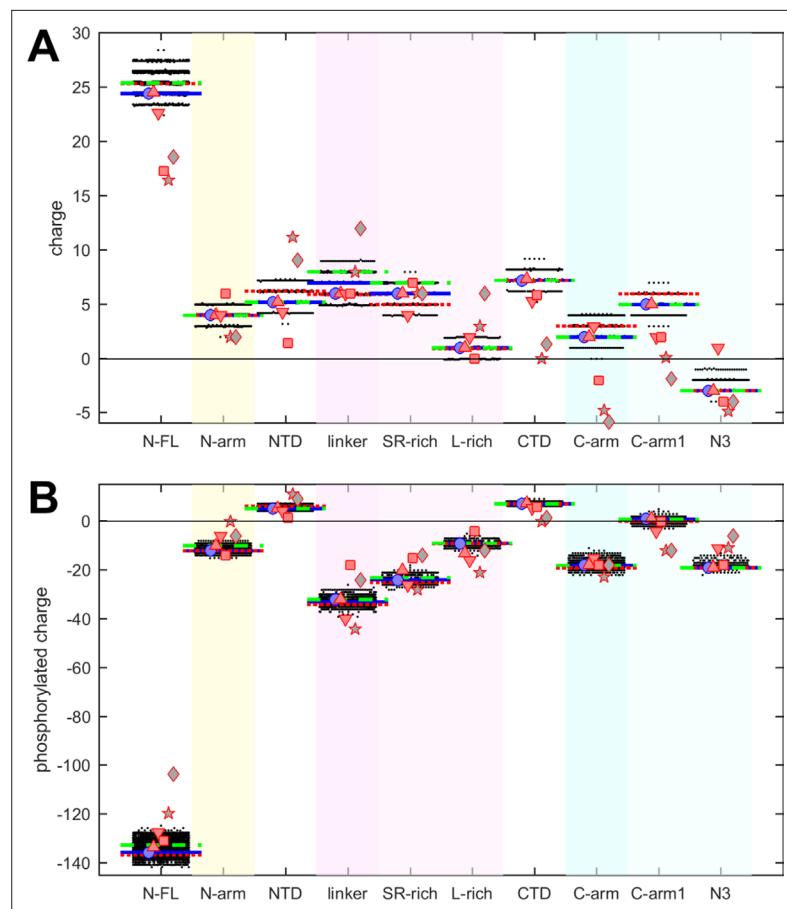
Figure 3. Beehive plots showing the distributions of charges of viable N-protein species. (**A**) Charges were calculated based on the amino acid composition of different N-protein regions as in *Figure 2*. Highlighted by horizontal lines are the values for the corresponding peptides from the ancestral sequence Wuhan-Hu-1 (blue), and including the defining mutations of the Delta variant (dotted red) and the Omicron variant (dashed green), respectively. Symbols indicate values for SARS-CoV-2 (ancestral sequence, blue circles), SARS-CoV-1 (red up triangles), Middle East respiratory syndrome coronavirus (MERS) (red down triangles), murine hepatitis virus (MHV) (red squares), NL63 (gray pentagrams), and bat coronavirus APD51511.1 (gray diamonds). (**B**) Same as in (**A**), with added charges from maximally phosphorylated serine, threonine, and tyrosine residues in the intrinsically disordered regions (IDRs).

via hydrophobic interactions to form coiled-coil oligomers that contribute to the architecture of RNPs in viral assembly (*Adly et al., 2023*; *Zhao et al., 2024*; *Zhao et al., 2023*).

Similarly, the C-arm IDR can be subdivided into the N3 region (N:390–419) and the remainder ('C-arm1', N:364–389), which also have strikingly different properties (*Figure 2*, blue arrows in cyan shaded columns): Whereas the connecting C-arm portion is by far the most polar, the N-terminal N3 region is among the most hydrophobic regions of the entire protein. Interestingly, the N3 region contains a transient helix (*Cubuk et al., 2021*; *Zhao et al., 2023*; *Zhao et al., 2022*), which may be involved in recognition of the packaging signal and M-protein interactions localized here (*Kuo et al., 2016*; *Masters, 2019*). Again, the difference in the physicochemical properties of these regions persists throughout the entire ensemble of sequences despite their significant spread and high mutation frequencies (*Figure 1B*).

Charges in proteins can control multiple properties related to electrostatic interactions, from functions of active sites to protein solubility, protein interactions, and conformational ensembles in IDRs (*Garcia-Viloca et al., 2004*; *Gerstein and Chothia, 1996*; *Gitlin et al., 2006*; *Mao et al., 2010*). The net charges of the different N-protein regions at pH 7.4 are displayed in *Figure 3A*. Similar to polarity and hydrophobicity, viable sequences can have significant spread of net charges among all the mutants, amounting to departures by ±(1–2) from the ancestral sequence. This is expected

considering the replacement and introduction of charged residues in the mutational landscape, e.g., including those from the defining substitutions of variants. The positive charge of the overall basic protein is shared similarly among all folded domains and IDRs. However, noteworthy is again the contrast arising from subdivision of the linker and C-arm, which displays uneven and non-overlapping distributions: despite the strongly basic character of the linker, its L-rich sequence is nearly neutral; similarly, the basic C-arm splits into an even more basic C-arm1 and an acidic N3 tail region. These differences are highly significant and persist throughout the mutant spectrum.

It is well established that intracellular N-protein can be heavily phosphorylated (in contrast to N-protein in the virion) (*Botova et al., 2024*; *Carlson et al., 2020*; *Fung and Liu, 2018*; *Johnson et al., 2022*; *Yaron et al., 2022*). As reviewed in *Yaron et al., 2022*, most serine, threonine, and tyrosine residues in the disordered regions (30 of 37) have been found phosphorylated in different proteomic analyses. Accordingly, we estimated the maximum charge when all of these residues in the IDRs are phosphorylated (*Figure 3B*). This leads to a negative charge for all IDRs. As might be expected, the largest impact was found in the SR-rich region of the linker, which carries the highest density of phosphorylation sites. Interestingly, despite the considerable spread of net charges within families of mutant sequences, the differences between the regions remain highly significant.

It is noteworthy that the defining mutations of the Delta and Omicron variant (denoted by dotted red and dashed green horizontal lines, respectively) do impact the hydrophobicity, polarity, and charges in all of the N-protein regions. However, their values do not stand out from the clouds of values across the mutant spectrum, which include more extreme values throughout.

Physicochemical properties of related coronaviruses

The distinct physicochemical properties of the linker and C-arm sub-segments persist throughout the mutant spectrum, which suggests these constitute biophysical constraints for functional SARS-CoV-2 N-protein. Therefore, we asked whether this holds true for N-protein from related coronaviruses such as SARS-CoV-1 (P59595.1), Middle East respiratory syndrome coronavirus (MERS, YP_009047211.1), murine hepatitis virus (MHV, NP_045302.1), human coronavirus NL63 (Q6Q1R8.1), and the 229E-related bat coronavirus APD51511.1. To this end, we used alignment of their consensus sequences to SARS-CoV-2 N-protein (shown previously; *Zhao et al., 2022*) to subdivide all N-proteins into equivalent regions (*Supplementary file 1*). As shown in *Table 1*, the resulting peptides present high sequence identity scores for the FL protein and the folded domains, but, with exception of SARS-CoV-1, have little to no sequence identity in the IDRs. This observation is consistent with the high mutation frequency of the IDRs.

The resulting peptides were subjected to the same analyses of physicochemical properties described above for SARS-CoV-2 N-protein. The results are displayed in *Figures 2 and 3* as symbols. With regard to hydrophobicity (*Figure 2B*), the FL proteins and folded domains show values within the range of the SARS-CoV-2 mutant spectrum. By contrast, more significant spread is observed in most IDR peptides. Nonetheless, the pattern observed for SARS-CoV-2 of hydrophobicity and polarity values of IDRs relative to those of the folded domains, and the pattern comparing subdivisions of the IDRs is closely mirrored for SARS-CoV-1, MERS, and MHV (red symbols). Similar patterns, although with some divergence, are observed for the NL63 and APD51511.1 IDRs (gray pentagrams and diamonds, respectively) which have the least sequence identity to SARS-CoV-2.

Table 1. Sequence alignment score of segments from related coronaviruses.

Virus	Full-length	N-arm	NTD	Linker	SR-rich	L-rich	CTD	C-arm	C-arm1	N3
SARS-CoV-1	672[*]	68.6	263	41.6	44.7	30	231	60.5	75.3	77
MERS	276	13.9	157				112	14.6	23.5	
MHV	192		114	14.6			80.5	14.6	13.4	
NL63	67.4		58.9				61.6			
APD51511.1	61.2		44.3				44.3			

*Values are BLASTp total alignment scores.

Table 2. Overview of N-protein species compared in biophysical experiments.

Designation	N-protein mutations	n exclusive instances*	Occur in # of distinct sequences[†]	Occurs in % of all genomes [‡]	In set of defining VOC mutations [§]
N:R203K/G204R	R203K, G204R	53,282	17,552	57%	α, γ, o
N:P13L/Δ31–33	P13L, Δ31–33	9548	12,503	47%	o
N_o	P13L, Δ31–33, R203K, G204R	791,613	10,238	46%	o (all BA.1)[¶]
$N_δ$	D63G, R203M, G215C, D377Y	$>1.2 \times 10^6$	9397	33%	δ (all 21J)[¶]
N:G215C	G215C	60	10,562	34%	δ
N:D63G	D63G	182	12,443	36%	δ
N_{ref}	none	38,929	NA	3.6%	NA

*Number of genomes where the indicated mutations are the only N mutations.
[†]Number of unique N-protein sequences in which indicated mutations are present, alongside other mutations.
[‡]Percentage of all sequenced genomes carrying the specific mutation.
[§]Variants of concern for which indicated mutations are part (or all) of the defining set of N-m.
[¶]These sets of mutations comprise all defining N-protein mutations of this variant. Literature on definition or biophysical characterization of the mutant.

Polarity values (*Figure 2A*) of all coronavirus linker peptides are higher than either their corresponding FL, NTD, or CTD regions. The subdivision of the linker in the peptides corresponding to SR-rich and L-rich regions of SARS-CoV-2 follow the same qualitative trend, with higher polarity in the equivalent SR-rich and lower polarity in the equivalent L-rich peptides for all coronaviruses studied. Similarly, the properties of the equivalent C-arm and subdivision of C-arm1 and N3 peptides for SARS-CoV-1, MERS, and MHV (red symbols) closely track the values from the mutant spectrum of SARS-CoV-2, although this is not the case for the more distant NL63 and APD51511.1 (gray symbols).

Charge properties of related coronaviruses follow a similar pattern of SARS-CoV-2 (*Figure 3A*), although with somewhat greater differences, particularly again for NL63 and APD51511.1. Peptides corresponding to L-rich regions exhibit low charge, distinctly below those of the SR-rich regions, and similarly, N3 peptides have lower charges than C-arm-1 peptides of the corresponding viral species, and nearly all are acidic. Even though it is unclear to what extent IDRs of other coronaviruses can be phosphorylated, their amino acid composition would provide similar potential as SARS-CoV-2, as the completely phosphorylated charges of all peptides follow closely those of SARS-CoV-2 (*Figure 3B*).

This suggests that the charge properties and phosphorylation, like polarity and hydrophobicity, of the equivalent IDR sub-regions are functional biophysical constraints maintained across related coronaviruses despite little sequence conservation.

Biophysical properties of select mutants

Unfortunately, it is impossible to express and experimentally characterize biophysical properties of all mutant species. Therefore, to assess the range of phenotype variation, we examine only six exemplary protein constructs related to variants of concern in comparison with the Wuhan-Hu-1 reference molecule, N_{ref} (*Table 2*): (1) N:R203K/G204R with a double mutation in the disordered linker that arose early in the Alpha variant (B.1.1.7), but occurs also in the Gamma variant (P.1), and all Omicron variants (BA.1 through BA.5). It was found to modulate phosphorylation of cytosolic N-protein, enhance assembly in a VLP assay, and increase viral fitness (*Johnson et al., 2022*; *Javed et al., 2023*; *Syed et al., 2022*); (2) N:P13L/Δ31–33 carrying the mutation P13L and the deletion Δ31–33 that are part of the defining mutations of all Omicron variants, with P13L epidemiologically ranked as the most statistically significant N-protein mutation linked to increased fitness (*Obermeyer et al., 2022*; *Oulas et al., 2021*); (3) N_o is a combination of N:R203K/G204R and N:P13L/Δ31–33, carrying thereby the complete set of defining mutations of the BA.1 Omicron variant; (4) N:G215C with a key mutation in the disordered linker that was associated with the rise of the 21J clade of the Delta variant, and found to modulate a transient helix in the L-rich linker region (*Zhao et al., 2022*). In a reverse genetics system, N:G215C was recently reported to cause significantly increased viral growth and altered virion morphology (*Kubinski et al.,*

2024). (5) N:D63G containing another defining mutation of the Delta variant, located in the NTD and epidemiologically ranked above G215C in increasing SARS-CoV-2 fitness (*Obermeyer et al., 2022*); and (6) N_δ carrying all four defining mutations D63G, R203M, G215C, D377Y of the Delta variant. As detailed in *Table 2*, all of these species are found in the genomic database, and in combination with additional mutations occur in a high fraction of all genomes (exceeding the frequency of the ancestral Wuhan-Hu-1 N-protein by an order of magnitude). However, with the exception of N:G215C, none of the mutants has been studied in detail with regard to their macromolecular biophysical properties.

All mutations considered here are within the IDRs, except for N:D63G, a mutation characteristic of the Delta variant. The presence of the N:D63G mutation in the NTD is highlighted in the shift of the intrinsic fluorescence quantum yield of this mutant in comparison to N_{ref} (*Figure 4A*). This may be attributed to changes in the local environment of tryptophan W108, which is partially surface exposed and structurally near the aspartic acid D63, as indicated by AlphaFold structural predictions (*Figure 4—figure supplement 1*). D63G ablates a negative surface charge near the NA binding site of the NTD, which poses the question whether this mutation alters NA binding affinity. We assessed this using sedimentation velocity analytical ultracentrifugation (SV-AUC) with the oligonucleotide T_{10} as an NA probe. T_{10} is comparable in length to the NTD binding canyon for NA but does not permit multi-valent binding (*Dinesh et al., 2020*; *Zhao et al., 2021*). No significant differences in the intrinsic binding affinity to T_{10} was detected between N:D63G, other mutants, and the ancestral species (*Figure 4—figure supplement 2*).

A parameter of great interest from an evolutionary perspective is the thermal stability of the folded domains. This property can be assessed experimentally by differential scanning fluorometry (DSF), which reports on temperature-driven changes in the environment of aromatic amino acids due to changes in solvent exposure (*Eftink, 2000*). Such changes may occur during unfolding or as a result of other conformational changes. In the case of N-protein, conveniently all tryptophan and tyrosine residues of N-protein are located in the NTD and CTD, such that changes in the intrinsic fluorescence report exclusively on changes in the state of the folded domains. As shown in *Figure 4B*, a major transition is observed with an inflection point at $T_i \approx 49°C$. Compared to the reproducibility of transition temperatures of ±0.3°C, significant shifts from the ancestral N-protein can be discerned: While Omicron mutations N_o, N:R203K/G204R, and N:P13L/Δ31–33 are neutral, those occurring in the Delta variant (N:D63G, N:G215C, and N_δ) are destabilizing, i.e., they lower the transition temperature. Interestingly, apparent destabilization of the folded domains occurs in N:G215C despite the absence of mutations in the folded domains – 215C being located in the middle of the linker IDR. This nonlocal mutation effect points to altered intra-molecular interactions between IDRs and the folded domains, and/or changes in contacts between folded domains mediated through an altered oligomeric state. (This is corroborated in non-natural point mutants N:L222P and N:L222P/R226P which abrogate linker helix oligomerization [*Zhao et al., 2023*] and exhibit T_i-values of ≈51°C.) Furthermore, *Figure 4B* shows additional transitions occur at higher temperatures broadly in the range of 60–70°C. While their origin is unclear, this signal may accompany the formation of higher-order structure. It is noteworthy that N:G215C is also distinctly different in this feature.

Secondary structure information from the entire molecule including the IDRs can be extracted from circular dichroism (CD) spectra. As may be observed from *Figure 4C* (and in more detail in *Figure 4—figure supplement 3*), significant variation occurs both in the magnitude of the negative ellipticity at ≈200 nm, which mainly reflects disordered residues, and in the magnitude of the negative ellipticity at ≈220 nm, which reports on helical structure. Compared to the ancestral N_{ref}, significantly less disorder and greater helicity is observed for N:G215C (and to lesser extent also for N_δ), whereas slightly more disorder is indicated for N:R203K/G204R. Little difference to the ancestral molecule is observed for N_o, N:P13L/Δ31–33, and N:D63G. The absence of significant changes for N:D63G is consistent with this mutation having only a subtle, if any, impact on the NTD conformation. For N:G215C, increased helicity can be attributed to the stabilization of transient helices in the leucine-rich region of the central linker IDR, as shown previously (*Zhao et al., 2023*; *Zhao et al., 2022*).

Tertiary and quaternary structure can be assessed by SV-AUC (*Figure 5A*). As reported previously, the ancestral N-protein at micromolar concentrations in NA-free form is a tightly linked dimer sedimenting at ≈4 S, without significant populations of higher oligomers (*Forsythe et al., 2021*; *Ribeiro-Filho et al., 2022*; *Tarczewska et al., 2021*; *Zhao et al., 2022*; *Zhao et al., 2021*). The same behavior is observed for N:D63G, N_o, N:R203K/G204R, as well as N:P13L/Δ31–33 at low micromolar
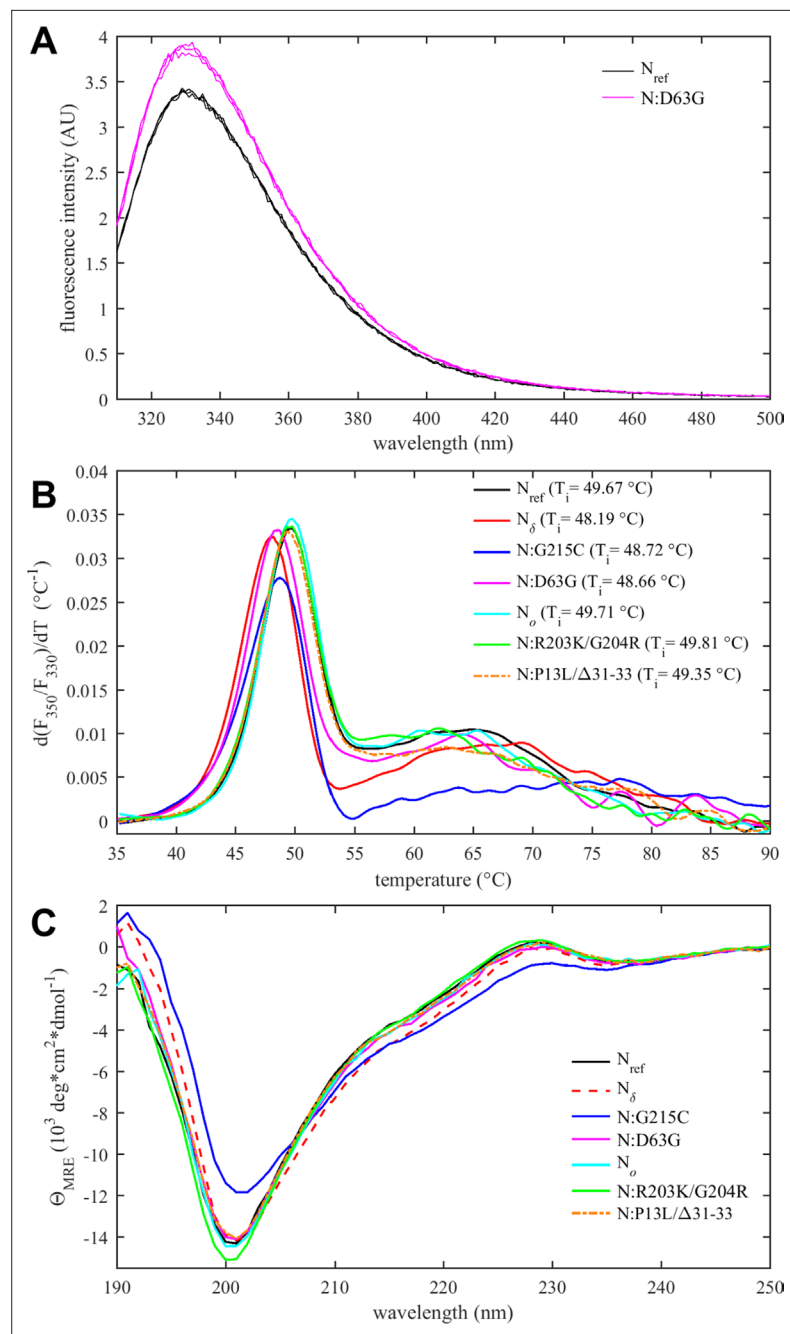
Figure 4. Thermodynamic stability and structural differences of N-protein reference and mutant species. (**A**) Intrinsic fluorescence spectrum of N:D63G in comparison with N_{ref}, showing spectra in triplicate. (**B**) Differential scanning fluorometry, with the temperature of maximum fluorescence ratio derivative (T_i-values, with an estimated precision 0.3°C). (**C**) Circular dichroism spectra of all N-protein species (spectra with error bars are shown in *Figure 4—figure supplement 3*).
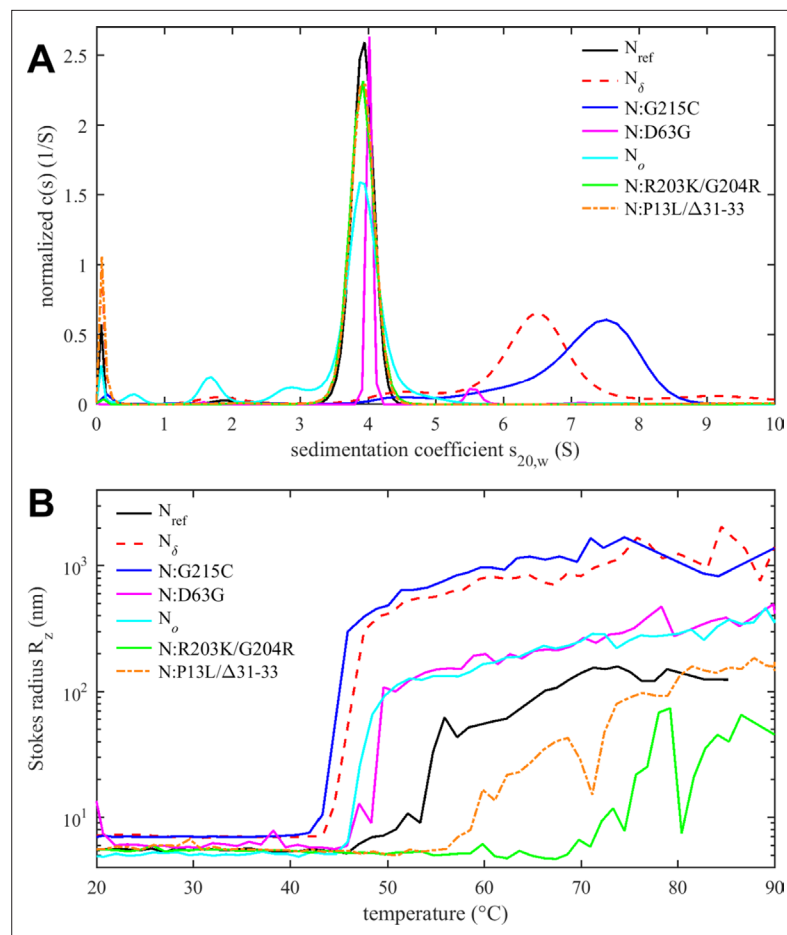
The online version of this article includes the following figure supplement(s) for figure 4:

Figure supplement 1. Structural comparison of N:D63G mutant and ancestral N-protein.

Figure supplement 2. N-protein affinity for binding nucleic acids (NA) probed by sedimentation velocity analytical ultracentrifugation (SV-AUC) of N-protein mixtures with oligonucleotide T_{10}.

Figure supplement 3. Individual comparison of circular dichroism (CD) spectra.

Figure supplement 4. Comparison of differential scanning fluorometry (DSF) data of N-protein species in low-salt (LS) and high-salt (HS) buffer.

Figure 5. Tertiary and quaternary structure of N-protein species. (**A**) Sedimentation coefficient distributions $c(s)$ from sedimentation velocity analytical ultracentrifugation (SV-AUC) experiments show ≈4 S dimers and higher oligomers. Data for N:G215C and N_δ are reproduced from *Zhao et al., 2022*. (**B**) Temperature-dependent particle formation reported as average Stokes radius measured by dynamic light scattering.

The online version of this article includes the following figure supplement(s) for figure 5:

Figure supplement 1. Comparison of solution state of N-protein species in low-salt (LS) and high-salt (HS) buffer.

---

concentrations (*Figure 5A*). By contrast, the G215C mutation promotes the formation of higher oligomers via stabilization of coiled-coil interactions of transient helices in the L-rich linker region (*Zhao et al., 2023*; *Zhao et al., 2022*). This is consistent with the enhanced helical content of this mutant (*Figure 4C*). Oligomerization beyond the dimeric N_{ref} is also observed for N_δ, which incorporates the 215C mutation, but less than for N:G215C. This is consistent with the intermediate helical content of N_δ observed in CD. Of the three additional mutations of N_δ relative to N:G215C, we speculate that D63G does not impact dimerization (as in N:D63G, *Figure 5A*), and that therefore either the distant D377Y and/or R203M might cause this reduction of helicity and oligomerization relative to N:G215C, noting that R203M is proximal to the L-rich region (215–235) reshaped by 215C (*Zhao et al., 2023*).

As outlined in the Introduction, N-protein has a propensity to form large particles and undergo LLPS (*Carlson et al., 2020*; *Cascarina and Ross, 2022*; *Cubuk et al., 2021*; *Iserman et al., 2020*; *Jack et al., 2021*; *Lu et al., 2021*; *Perdikari et al., 2020*; *Savastano et al., 2020*), which can be promoted at higher temperatures (*Iserman et al., 2020*; *Zhao et al., 2021*). *Figure 5B* shows the z-average particle size measured by dynamic light scattering (DLS) as a function of temperature. Particle formation is governed by a combination of processes, including the hydrophobicity-driven stabilization of the linker helix and its self-association, ultra-weak interactions across the entire protein contributing to LLPS, and unfolding and aggregation processes. This complicates a comparison of the temperature transitions observed in DSF (*Figure 4B*) and DLS (*Figure 5B*) (and a further technical difficulty may

be potential differences in temporal lag of conformational rearrangements versus particle assembly kinetics).

Nevertheless, several clear observations can be made. As reported previously, N_{ref} forms clusters and particles at >55°C (*Zhao et al., 2021*), which is strongly enhanced and occurs at a lower temperature for N:G215C, due to the enhancement of the linker oligomerization (*Figure 5B*; *Zhao et al., 2023*). Very similar behavior is observed for N_δ, which suggests that at higher temperatures any potential inhibitory role suspected of the R203M mutation on self-association may be less relevant compared to G215C. It is interesting to note that, correspondingly, both show a lower T_i in DSF. More moderate enhancement of particle formation is observed for N:D63G, which shows an onset already at ≈50°C and larger particle averages than the ancestral protein. This also correlates with its significantly lower T_i in DSF. Thus, even subtle structural changes (as shown in *Figure 4—figure supplement 1*) can impact the assembly behavior.

The opposite effect, strong inhibition of particle formation, is observed for the N:R203K/G204R double mutant. Here, particles form only at temperatures >70°C, as a mixture of smaller clusters with some very large aggregates that adventitiously enter the light path in DLS and cause fluctuations in the *z*-average Stokes radius. Interestingly, although N_o comprises the R203K/G204R mutation, N_o does not share this behavior but instead exhibit slightly enhanced particle formation relative to the ancestral N_{ref}, comparable to N:D63G. This points to the role of additional mutations in N_o, which besides R203K/G204R features the N-arm mutations P13L and Δ31–33. Interestingly, by themselves in N:P13L/Δ31–33 the particle formation is also suppressed relative to N_{ref}, although less so than for N:R203K/G204R. This again points to non-additive effects, suggesting that the combination of N-arm and linker IDR mutations in N_o alter the effect of either set of inhibitory mutations alone, to jointly promote particle formation of N_o.

We were curious whether IDR mutations might alter particle formation through modulation of existing or introduction of new protein-protein interfaces. We focused on Omicron mutations as these are obligatory in all currently circulating strains, and specifically on N-arm mutations, which have recently been implicated in altered intramolecular interactions with NA-occupied NTD (*Cubuk et al., 2023*). Even though SV-AUC showed no indication of self-association of N:P13L/Δ31–33 at low micromolar concentrations, weak interactions with K_d > mM would not be detectable under these conditions yet could be highly relevant in the context of multi-valent complexes (*Zhao et al., 2024*). Following the roadmap used previously for the study of the weak self-association of the leucine-rich linker IDR (*Zhao et al., 2023*), we restricted the protein to the N-arm peptide such that it can be studied at much higher concentrations. To this end, we compared solution behavior of the N-arm constructs N_{ref}:(1–43) with the Omicron N-arm N:P13L/Δ31–33(1–43), as well as the N-arm with individual mutation N:P13L(1–43) and deletion N:Δ31–33(1–43). Unexpectedly, solutions of N:P13L/Δ31–33(1–43) exhibited elevated viscosity after storage for several days at 4°C in 20 mM HEPES, 150 mM NaCl, pH 7.5. Since this is a tell-tale sign of weak protein interactions, we carried out ColabFold structural predictions. Even though ColabFold is trained to predict folded structures, it has been found to be frequently successful in predicting transient folds in IDRs (*Alderson et al., 2023*; *Zhao et al., 2023*). Indeed, it predicts that replacement of proline at position 13 by leucine allows for formation of parallel sheets symmetrically arranged in higher-order N-arm oligomers (*Figure 6—figure supplement 1*). We proceeded to test oligomerization of the N-arm constructs experimentally in hydrodynamic studies. *Figure 6A* shows autocorrelation functions of all peptides. While the reference N-arm N_{ref}:(1–43) and the construct carrying the Δ31–33 deletion behave as expected for non-interacting peptides of this size, the N-arm constructs carrying the P13L mutation (in particular, the Omicron N-arm N:P13L/Δ31–33(1–43)) exhibit very large correlation times. This may be indicative of either formation of large particles or the presence of weak interaction networks as in gels. Similarly, in SV-AUC (*Figure 6B*) the ancestral reference and the Δ31–33 deletion mutant sediment as expected for non-interacting N-arm peptides (*Zhao et al., 2023*), whereas rapidly sedimenting, anomalously shaped boundaries with ≈100-fold larger sedimentation coefficient were observed for the Omicron N-arm and the construct carrying solely the P13L mutation. This unequivocally demonstrates the introduction of new protein self-association interfaces from the P13L mutation. They are weak and not apparent in studies of the full-length protein N:P13L/Δ31–33 at low micromolar concentrations, but oligomers can be populated at the ≈100-fold higher achievable concentrations of the peptides, which mirrors the concentration range for in vitro observation of interactions of the leucine-rich linker helices (*Zhao et al., 2023*).
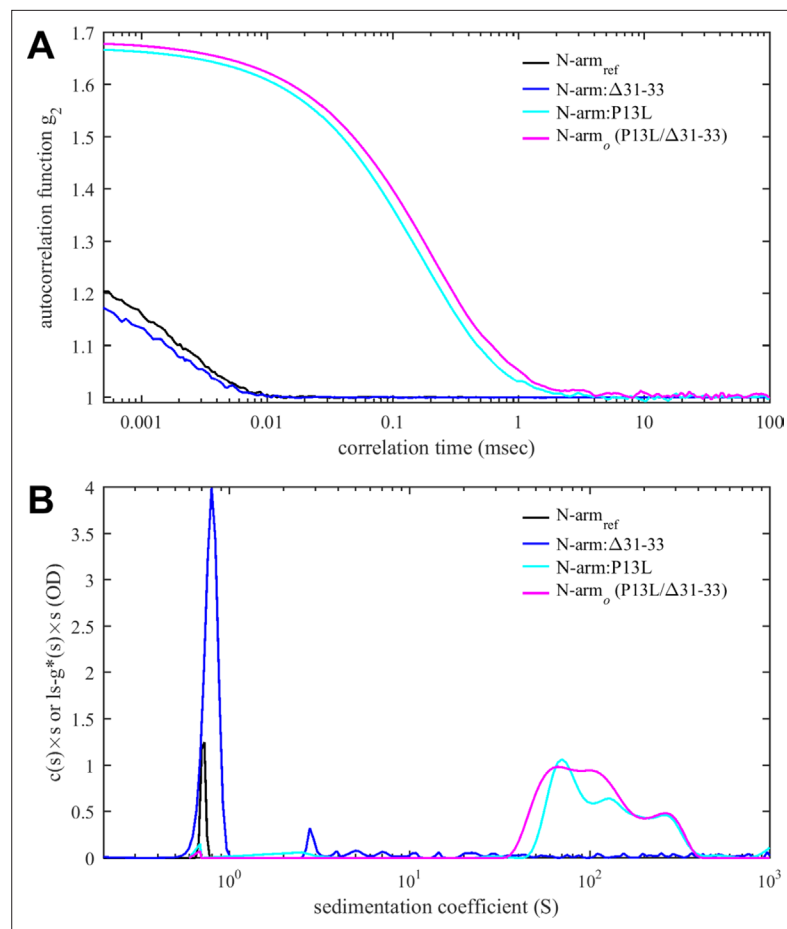
Figure 6. Protein-protein interactions of N-arm peptide containing the Omicron P13L mutation lead to large structures at high concentrations. (**A**) Autocorrelation functions from dynamic light scattering (DLS) (**A**) and sedimentation coefficient distributions from sedimentation velocity analytical ultracentrifugation (SV-AUC) (**B**) for the ancestral reference N_{ref}:(1–43) (black), N:Δ31–33(1–43) (blue), N:P13L(1–43) (cyan), and N:P13L/Δ31–33(1–43) (identical to the Omicron N-arm, magenta). All peptide concentrations are 400 µM, except for N_{ref}:(1–43) in the SV-AUC experiment which is 275 µM, reproduced from previously reported data (***Zhao et al., 2023***).

The online version of this article includes the following figure supplement(s) for figure 6:

Figure supplement 1. Structural prediction of Omicron N-arm self-interactions.

The ability for N-protein to undergo LLPS is thought to be crucial for several functions including interactions with stress granules, RNP assembly, and interactions with viral M-protein (***Carlson et al., 2022***; ***Cascarina and Ross, 2022***; ***Iserman et al., 2020***; ***Lu et al., 2021***; ***Savastano et al., 2020***). Weak protein-protein interactions and cluster formation such as shown in ***Figures 5 and 6*** can be coupled to LLPS, or alternatively LLPS may occur independent of clusters following Flory-Huggins theory (***Kar et al., 2022***). Therefore, we examined the impact of mutations on the propensity for LLPS. Images of phase-separated condensates are shown in ***Figure 7***, and corresponding histograms of droplet numbers and areas are shown in ***Figure 7—figure supplement 1***. As may be discerned from the top left panel of ***Figure 7***, N_{ref} readily forms droplets in the presence of T_{40} oligonucleotides. Under the same conditions, N:R203K/G204R (bottom left) does not display droplets, but forms few large particles with fibrillar morphology. In stark contrast, N:P13L/Δ31–33 (bottom center) readily forms droplets that appear to be more rapidly merging and growing than those of N_{ref} (***Figure 7— figure supplement 2***). The combination of these mutations in N_o exhibits an intermediate propensity for LLPS with droplets in a dispersion of sizes. The most polydisperse distribution with largest droplets were observed for N:G215C (***Figure 7—figure supplement 1***).
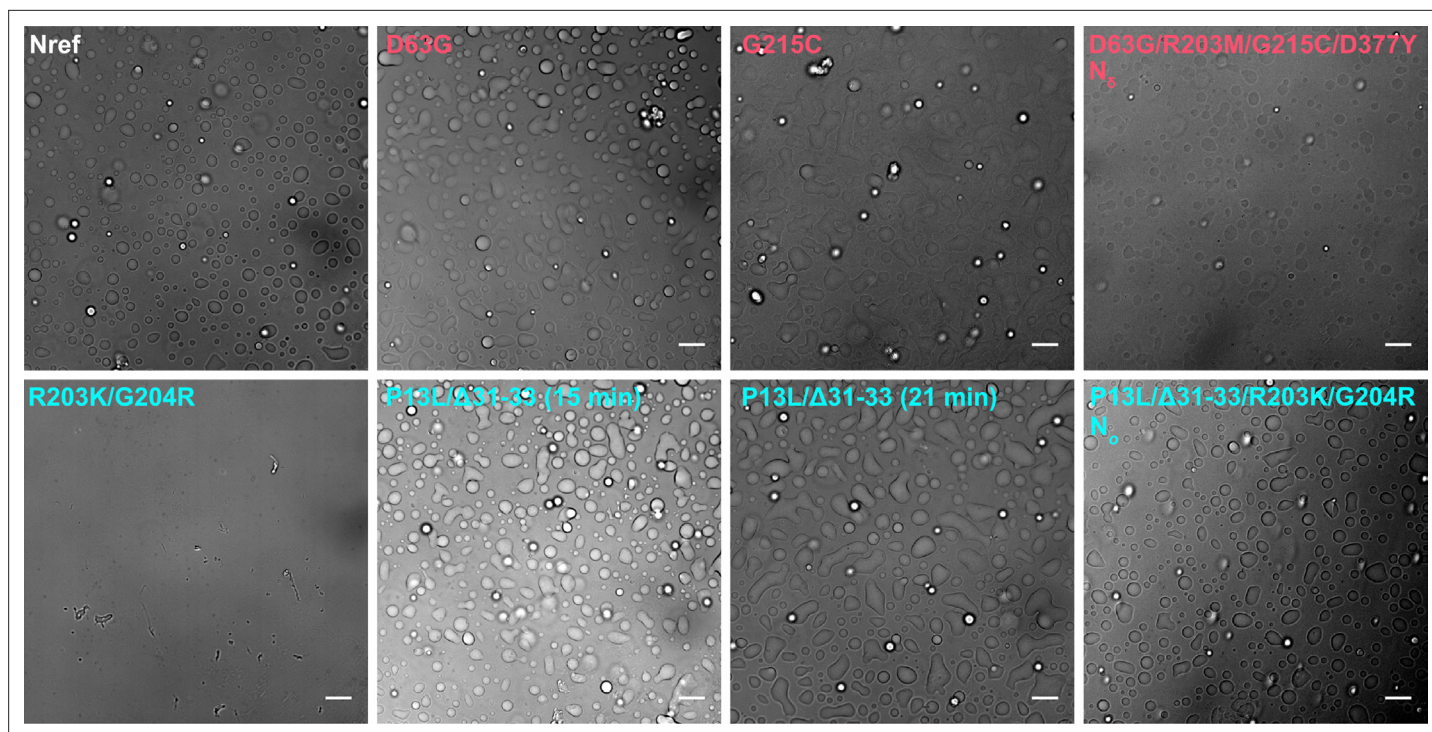
Figure 7. Differences in liquid-liquid phase separation (LLPS) propensity of N-protein mutant species. Optical microscopy images were taken of 10 μM N-protein with 5 μM T_{40} (except N_δ, which is 4 μM N-protein with 2 μM T_{40}) in low-salt (LS) buffer after incubation for 15 min at room temperature. For N:P13L/Δ31–33, a second image was taken at the 21 min time point highlighting the growth of condensed phases. All scale bars are 10 μm. Histograms of particle areas are in *Figure 7—figure supplement 1*, and a comparison of two time points for N_{ref}, N:R203K/G204R and N:P13L/Δ31–33, is provided in *Figure 7—figure supplement 2*.

The online version of this article includes the following figure supplement(s) for figure 7:

Figure supplement 1. Comparison of area distributions of droplets in images of *Figure 7*.

Figure supplement 2. Comparison of droplet area after liquid-liquid phase separation (LLPS) at two points in time.

Discussion

The SARS-CoV-2 pandemic has motivated the collection of virus genomic sequences on an unprecedented scale, which has generated invaluable data on the genomic diversity of an RNA virus. From the ensemble of observed consensus sequences of infected hosts, we can extract, for the first time, an exhaustive map of possible amino acid replacements in viral proteins that are tolerable for viable virus (*Bloom et al., 2023*; *Saldivar-Espinoza et al., 2023*; *Zhao et al., 2022*). This brings into stark relief our limited understanding of the genotype/phenotype relationship, which is very detailed on some local functional aspects, such as spike protein antigenicity, but not much developed in general. This limits our ability to draw conclusions from the observed mutant spectrum on their variation in biophysical functions and fitness. Besides traditional sequence-based structure prediction and structure/function relationships, and more recent recognition of structural dynamics, new paradigms have emerged with increased understanding of the role of IDRs, their mimicry of SLiMs, nonlocal physicochemical properties of sequence regions, and the ability of IDRs to promote macroscopic phase separation to generate or usurp condensates with virus-related functions. The extensive genomic data of SARS-CoV-2 presents an opportunity to probe how sequence diversity impacts these biophysical properties, and to examine what biophysical constraints exist for viral proteins to support viability. Focusing on SARS-CoV-2 N-protein we have studied the diversity of biophysical phenotypes with the goal to increase understanding of salient mechanisms of the many N-protein functions, and also to glean aspects of the biophysical fitness landscape underlying evolution.

On one hand, our studies of the diversity of nonlocal physicochemical properties of N-protein revealed the absence of tightly controlled hydrophobicity, polarity, and charges outside the folded domains. In the IDRs, individual mutations may alter each of these properties apparently without

impacting viability, although modulatory fitness effects may be possible. For example, viable linker sequences span from 4.8 to 9.1 charges. On the other hand, a very clear separation of physicochemical parameters far exceeding mutational dispersion is maintained between the L-rich and SR-rich region of the linker IDR, and between the N3 and remaining region of the C-arm IDR. These distinctions are likely functionally important, with the polarity and charges of the SR-rich linker region aiding in NA binding (*Pontoriero et al., 2022*), the hydrophobicity of the L-rich region aiding in assembly functions (*Bessa et al., 2022*; *Zhao et al., 2024*; *Zhao et al., 2023*), and the acidic N3 region probably playing a role in NA- and M-protein interactions as suggested from analogy to MHV- and SARS-CoV-1 (*Masters, 2019*). These nonlocal features are also maintained in analogous consensus sequence regions of related coronaviruses, and thus provide further examples for nonlocal biophysical properties that are evolutionary conserved despite amino acid sequence divergence (*Zarin et al., 2017*; *Zarin et al., 2021*). It may seem as a paradox that despite this conservation these features seem not very fine-tuned and that significant variation of these properties is still observed within the viable mutant spectrum, for polarity and hydrophobicity significantly exceeding the spread of parameter values of the folded domains. However, as mentioned above, the differences between IDR regions that appear associated with biophysical functions are of significantly larger magnitude. The tolerance for the remaining comparatively smaller fluctuations in physicochemical parameters may be important to allow sufficient local variation in sequence space for additional functions to evolve, such as the emergence of SLiMs to manipulate the host/virus interface (*Davey et al., 2011*; *Schuck and Zhao, 2023*). Correspondingly, in a recent study of SLiMs variation across the mutant spectrum, we found the total number and detailed location of phosphorylation SLiMs to vary considerably in the SR-rich region, but to be maintained overall at a high level across this region (*Schuck and Zhao, 2023*).

Other nonlocal properties were studied experimentally, though unavoidably only by example of several different SARS-CoV-2 N-protein species. We selected conspicuous mutations in variants of concern, but each of the constructs studied also represents in itself viable N-protein species occurring in consensus sequences of the genomic database. Strikingly, point mutations can affect protein properties on all levels of organization, from thermodynamic stability and secondary structure to intra- and inter-molecular interactions, oligomeric state, particle formation, and LLPS. These results must be considered in the context of the highly dynamic nature of N-protein, which is caused by the flexibility of intrinsically disordered domains (*Cubuk et al., 2023*; *Cubuk et al., 2021*; *Redzic et al., 2021*; *Zhao et al., 2021*), the NTD and its disordered β-hairpin (*Redzic et al., 2021*), and the large-scale conformational fluctuations of the N-protein dimer in solution (*Botova et al., 2024*; *Ribeiro-Filho et al., 2022*; *Różycki and Boura, 2022*). High sequence plasticity is accompanied by high plasticity of protein configuration and delicate balances of protein interactions that can be significantly shifted by single mutations with nonlocal effects.

Our results highlight two different mechanisms through which mutation effects may be propagated across the protein. First, mutations can impact the transient helix in the hydrophobic L-rich region of the linker, and, as we have shown previously, promote its helical conformation and self-association into higher oligomeric states (*Zhao et al., 2023*; *Zhao et al., 2022*). This, in turn, may impact collision frequency or other intra-molecular interactions with folded domains, such as the recently reported intra-molecular contact of the L-rich region to the NTD observed by NMR (*Botova et al., 2024*). This is reflected in the altered secondary structure observed in CD of N_δ and N:G215C, as well as their oligomers observed in SV-AUC, and this would explain the impact of the G215C mutation on the thermal stability reported by intrinsic fluorescence localized to the NTD and CTD. In addition, changes near the L-rich transient helix also impact weak protein interactions and amplify to enhanced particle formation and altered LLPS. Notably, introduction of N:G215C in a reverse genetics system resulted in enhanced viral replication and larger virions (*Kubinski et al., 2024*).

Second, mutation frequencies peak in the downstream end of the SR-rich linker region, including the double mutation R203K/G204R that is part of the defining mutations of Omicron (and other) variants. In different VLP and cellular assays (*Johnson et al., 2022*; *Syed et al., 2022*), it has been shown to modulate N-protein phosphorylation and thereby the balance between replication and assembly, with contributions from an emerging alternate, truncated N-protein (210–419) that itself supports assembly (*Adly et al., 2023*; *Leary et al., 2021*; *Mears et al., 2022*; *Javed et al., 2023*). In the present study, we found that full-length N:R203K/G204R strongly opposes both temperature-driven particle formation and LLPS with oligonucleotides. Interestingly, this effect can be compensated for

by the additional N-arm mutation P13L that is present in all Omicron variants. P13L itself has been identified epidemiologically as the most important driver of fitness in N-protein (*Obermeyer et al., 2022*; *Oulas et al., 2021*), but its biophysical effects have not been previously studied. We identified a distinct self-association propensity of N-arm peptides carrying the P13L mutation, and enhanced LLPS propensity of full-length N-protein carrying the complete set of N-arm mutations in Omicron, N:P13L/Δ31–33. This is consistent with the partial 'rescue' of particle formation and full restoration of LLPS propensity that we have observed in the N$_o$ molecule with the complete set of P13L/Δ31–33/R203K/G204R mutations defining N-protein from the BA.1 (B.1.1.529) Omicron variant. It is interesting to note that the R203K/G204R mutation, the P13L mutation, and the P13L/Δ31–33 combination each can occur independently of each other in viable virus species, with 261 genomes in the database carrying only the P13L mutation, 9548 only the combination P13L/Δ31–33, and >50,000 genomes exclusively the double mutation R203K/G204R, even though their more frequent coexistence (by approximately 10-fold, in all of Omicron variants) might suggest epistatic interactions and a fitness advantage. Relatedly, it was shown that the P13L mutation causes complete loss of recognition of a CD8+ T-cell epitope, which may cause T-cell evasion (*de Silva et al., 2021*), and provide an additional fitness effects of this mutation. Compensating effects between linker IDR and N-arm mutations highlight the nonlocal consequences of IDR mutations. They also highlight the difficulty of assigning variant properties and fitness effects to a single mutation, given the entangled effects among the sets of multiple mutations defining the variants of concern.

In summary, the importance of IDRs in viral evolution was recognized previously for several reasons. Their inherent flexibility makes them more permissible for amino acid changes, which is born out in the mutational landscape of SARS-CoV-2. As mentioned above, this makes them well suited for host adaptation through remodeling of host protein interaction networks, which is exemplified in the clusters of host-specific mutations located in IDRs of Dengue virus proteins (*Charon et al., 2018*; *Dolan et al., 2021*). Mimicry of eukaryotic SLiMs is ubiquitous (*Davey et al., 2011*; *Hagai et al., 2014*; *Mihalič et al., 2023*), and as we have shown recently, the sequence space of SARS-CoV-2 N-protein IDRs allows presentation of a large fraction of known eukaryotic SLiMs (*Schuck and Zhao, 2023*). In addition, nonlocal sequence-distributed physicochemical features of IDRs such as their charge and hydrophobicity have been demonstrated recently to mediate biological functions and present evolutionary constraints (*Moses et al., 2023*; *Zarin et al., 2021*). This principle also holds true in the distinct properties of linker and C-arm regions of SARS-CoV-2 N-protein. A related nonlocal physicochemical property of IDRs is their propensity for supporting LLPS (*Abyzov et al., 2022*; *Brocca et al., 2020*; *Pappu et al., 2023*), which plays a key role in different N-protein functions (*Carlson et al., 2020*; *Cascarina and Ross, 2022*; *Roden et al., 2022*; *Savastano et al., 2020*). Finally, here we have observed the ability of mutations in IDRs to modulate overall biophysical properties such as thermal stability, oligomeric state, and assembly properties. In SARS-CoV-2 N-protein IDRs, the latter are mediated via weak interactions in transiently folded structures. In addition, the high flexibility of the IDRs and their resulting high intra-chain contact frequencies (*Botova et al., 2024*; *Różycki and Boura, 2022*) may magnify nonlocal consequences of mutations. This endows viral protein IDRs with yet another level of variation of the biophysical phenotype that can impact evolutionary fitness. Exploiting the emerging mutational landscape and sequence space presents both a challenge and opportunity to explore the biophysical phenotype spectrum and thereby to uncover the salient functional principles of RNA-virus proteins.

Materials and methods
Mutational landscape, sequence alignment, and prediction of physicochemical properties

The Wuhan-Hu-1 isolate (GenBank QHD43423) (*Wu et al., 2020*) was used as the ancestral reference. Sequence data were based on consensus sequences of SARS-CoV-2 isolates submitted to the GISAID as previously described (*Schuck and Zhao, 2023*; *Zhao et al., 2022*). Briefly, sequence data were downloaded on January 20, 2023, from Nextstrain (*Hadfield et al., 2018*) and 5.06 million high-quality preprocessed sequences were included in the analysis. 746 sequences exhibiting insertions in the N-protein were omitted, as well as those with more than 10 deletions in N-protein and those represented in fewer than 10 genome instances.

The resulting sequence database was parsed for different unique sequences for N-proteins and different segments, using code written in MATLAB (MathWorks, Natick, MA, USA). Sequence hydrophobicity was calculated in RStudio (https://posit.co/) using the package PEPTIDES (*Osorio et al., 2015*) and polarity and charge using the package ALAKAZAM (*Gupta et al., 2015*). For maximally phosphorylated charge, –2 was added to the total charge for each serine, threonine, and tyrosine in the IDRs.

Alignment of SARS and related coronavirus sequences (SARS-CoV-1 P59595.1, MERS YP_009047211.1, MHV NP_045302.1, human coronavirus NL63 Q6Q1R8.1, and 229E-related bat coronavirus APD51511.1) was carried out with COBALT at NLM (*Papadopoulos and Agarwala, 2007*), as shown in *Zhao et al., 2022*. This alignment was used to dissect related viruses into regions corresponding to the SARS-CoV-2 regions (N-arm, NTD, linker, SR-rich, L-rich, CTD, Carm, Carm1, N3) (*Supplementary file 1*). The resulting segments of the related viruses were subjected to analysis of physicochemical properties as described above. Sequence similarity of the corresponding regions relative to the SARS-CoV-2 regions was calculated using BLAST blastp suite (*Altschul et al., 1997*), using an expectation threshold of 0.9, word size 2, and BLOSUM63 scoring matrix.

Structure prediction

Structural predictions for NTD and N-arm were carried out using ColabFold (*Mirdita et al., 2022*) and graphics were generated using ChimeraX (*Pettersen et al., 2021*).

Proteins, peptides, and oligonucleotides

N:D63G and N:G215C were purchased from EXONBIO (catalog# 19CoV-N170 and 19CoV-N180, San Diego, CA, USA), while N_{ref}, N:R203K/G204R, N:P13L/Δ31–33, N_o, and N_δ were expressed in-house as described previously (*Zhao et al., 2023*; *Zhao et al., 2022*). Briefly, the full-length protein with an N-terminal Tobacco etch virus (TEV) cleavage site and 6xHis tag was cloned into the pET-29a(+) expression vector and transformed into One Shot BL21(DE3)pLysS *Escherichia coli* (Thermo Fisher Scientific, Carlsbad, CA, USA). After cell lysis, the protein was bound to a Ni-NTA column, and unfolded and refolded to remove residual protein-bound bacterial NA (*Carlson et al., 2020*). After elution the 6xHis tag was cleaved and the protein purified by size exclusion chromatography. Greater than 95% purity of the proteins was confirmed by SDS-PAGE, and the ratio of absorbance at 260 nm and 280 nm of ~0.50–0.55 confirmed absence of NA. The latter is important to eliminate higher-order N-protein oligomers induced by NA binding (*Carlson et al., 2020*; *Tarczewska et al., 2021*; *Zhao et al., 2021*). For a subset of mutants, the protein sequence and mass were tested and confirmed by LC-MS/MS and LC-MS, respectively. Biophysical experiments were preceded by dialysis in either high-salt (HS) buffer consisting of 20 mM HEPES, 150 mM NaCl, pH 7.5, or low-salt (LS) buffer consisting of 10.1 mM Na_2PO_4, 1.8 mM KH_2PO_4, 2.7 mM KCl, 10 mM NaCl, pH 7.4 as indicated below.

The oligonucleotide T_{40} was purchased from Integrated DNA Technologies (Skokie, IL, USA), as purified by HPLC and lyophilized. N-arm peptides were purchased from ABI Scientific (Sterling, VA, USA), as purified by HPLC, examined by MALDI for purity and identity, and lyophilized.

Spectroscopy

CD spectra were acquired in a Chirascan Q100 (Applied Photophysics, UK), using cuvettes of 1 mm pathlength, and data acquisition with 1 nm steps and 1 s integration time. Results are averages of three acquisitions, corrected for buffer background. Protein concentration was 3 µM in buffer LS, except N_o in buffer HS.

For the acquisition of fluorescence spectra, protein samples at 1 µM were loaded into a quartz cuvette with 1.0 cm optical pathlength. Steady-state tryptophan fluorescence emission spectra in the range from 305 nm to 500 nm were recorded in a spectrofluorimeter (QuantaMaster, Photon Technology) with excitation at 295 nm using a 1.0 nm increment. Scans were acquired in triplicate.

DSF was carried out in a Tycho instrument (Nanotemper, Germany) as previously described (*Zhao et al., 2021*). Briefly, 10 µL samples were aspirated in capillaries (TY-C001, Nanotemper, Germany), and intrinsic fluorescence was measured at 350 nm and 330 nm while the temperature was ramped from 35°C to 95°C at a rate of 30°C/min. The first derivative of the intensity ratio was calculated as a function of temperature. DSF experiments were carried out at protein concentrations of 2 µM in buffer LS, except for N:R203K/G204R which was measured in buffer HS. As a buffer control, the difference

in T_i for N_{ref} in LS and HS buffer was measured and found to be within error of data acquisition (*Figure 4—figure supplement 4*).

Hydrodynamic techniques

SV-AUC experiments were carried out in a ProteomeLab XL-I analytical ultracentrifuge (Beckman Coulter, Indianapolis, IN, USA) in standard configurations (*Schuck et al., 2015*), with instruments subjected to routine calibrations (*Ghirlando et al., 2013*). Briefly, 2 µM protein samples were filled in cell assemblies composed of charcoal-filled Epon double-sector centerpieces with sapphire windows, inserted in an 8-hole AN-50 TI rotor and temperature equilibrated. After acceleration to 50,000 rpm data acquisition commenced using the absorbance optical detector at 280 nm and the interference optical detector. Data were analyzed in SEDFIT (https://sedfitsedphat.nibib.nih.gov/software/default.aspx) in terms of a sedimentation coefficient distribution $c(s)$ (*Schuck, 2016*). Proteins for self-association studies were in buffer HS, except N_{ref}, N_δ, and N:G215C were in LS, the latter causing an ≈5% increase in *s*-value (*Figure 5—figure supplement 1*). Typical accuracy of $c(s)$ peaks are on the order of ≈1% for peak *s*-values and ≈1–2% for relative peak areas (*Zhao et al., 2015*).

NA binding experiments were analyzed in buffer HS and LS with isotherms of signal weighted-average sedimentation coefficients in SEDPHAT (*Schuck and Zhao, 2017*). For studies of the N-arm peptide species, 400 µM peptide samples were studied by gravitational sweep sedimentation using rotor speed steps of 3000 rpm, 10,000 rpm, 40,000 rpm, and 55,000 rpm (*Ma et al., 2016*) and analyzed with a model for apparent sedimentation coefficient distributions $ls\text{-}g^*(s)$ (*Schuck, 2016*) as a qualitative representation of rapidly migrating boundaries of N:P13L(1:43) and N:P13L/Δ31-33(1:43), or with $c(s)$ distributions for N_{ref}:(1:43) and N:Δ31-33(1:43).

Temperature-dependent DLS autocorrelation data of N-protein species were collected in a NanoStar instrument (Wyatt Technology, Santa Barbara, CA, USA) equipped with a 658 nm laser and using a detection angle of 90°. 100 µL samples at 3 µL N-protein in LS buffer were inserted into a 1 µL quartz cuvette (WNQC01-00, Wyatt Instruments), with excess sample to prevent evaporation in the observation chamber. A temperature ramp rate of 1 °C/min was applied with 5 s data acquisitions and averaging three replicates for each temperature point. Data were collected and processed with the software Dynamics 7.4 (Wyatt Instruments) to determine the average hydrodynamic radius by cumulant analysis.

DLS studies of N-arm peptides were carried out in a Prometheus Panta (Nanotemper, Germany) instrument at 20°C. The samples were loaded into a capillary (Nanotemper PR-AC002) and ACFs were acquired using the 405 nm laser at the detection angle of 140°.

Optical microscopy

Optical imaging of in vitro phase-separated condensates was carried out as described previously (*Zhao et al., 2021*). Briefly, reaction mixtures of N-protein and T_{40} in buffer LS were combined and mixed immediately prior to imaging. 3µL samples were transferred onto a glass-bottom 35 mm dish (catalog# Part No: P35G-1.5–20-C, MatTek) for imaging at room temperature. Images were acquired on a Nikon Ti-E microscope equipped with a 100× 1.49 NA oil objective lens (LIDA light engine, Lumencor, Beaverton, OR, USA) and recorded with a Prime 95B camera (Teledyne Photometrics) with a pixel size of 110 nm. Images were background-subtracted and contrast-enhanced using MATLAB (Mathworks, Natick, MA, USA).

The segmentation of different shapes in the brightfield images was performed with deep learning methods. Specifically, a pre-trained model (versatile) from StarDist Napari Plugin (*Schmidt et al., 2018*) was employed to segment the shapes with the following parameters: Input image scaling: 0.5, probability threshold: 0.2, overlap threshold: 0.2. The labels were imported into Fiji and LABKIT (*Arzt et al., 2022*) for manual verification and correction. For each segmented object, the area was measured in MATLAB.

Materials availability

Plasmids for mutant N-proteins generated in this study are available from the author upon request.

Acknowledgements

Additional information

Funding

Author contributions

Ai Nguyen, Resources, Investigation, Methodology, Writing – review and editing; Huaying Zhao, Conceptualization, Data curation, Software, Formal analysis, Investigation, Methodology, Writing – review and editing; Dulguun Myagmarsuren, Sanjana Srinivasan, Investigation; Di Wu, Resources, Formal analysis, Investigation, Methodology, Writing – review and editing; Jiji Chen, Resources, Software, Investigation, Methodology, Writing – review and editing; Grzegorz Piszczek, Resources, Formal analysis, Supervision, Investigation, Methodology, Writing – review and editing; Peter Schuck, Conceptualization, Formal analysis, Supervision, Funding acquisition, Writing – original draft, Project administration, Writing – review and editing

Author ORCIDs

Huaying Zhao ⓘ https://orcid.org/0000-0002-8827-6639
Peter Schuck ⓘ https://orcid.org/0000-0002-8859-6966

Peer review material

Reviewer #2 (Public Review): https://doi.org/10.7554/eLife.94836.3.sa1
Reviewer #3 (Public Review): https://doi.org/10.7554/eLife.94836.3.sa2
Author response https://doi.org/10.7554/eLife.94836.3.sa3

Additional files

Supplementary files

• Supplementary file 1. Sequence alignment of nucleocapsid protein of related coronaviruses and sequences corresponding to SARS-CoV-2 regions. N-protein sequences of SARS-CoV-1 P59595.1, MERS YP_009047211.1, MHV NP_045302.1, human coronavirus NL63 Q6Q1R8.1, and 229E-related bat coronavirus APD51511.1 were aligned with SARS-CoV-2 N-protein. Regions corresponding to the SARS-CoV-2 regions (N-arm, NTD, linker, SR-rich, L-rich, CTD, Carm, Carm1, N3) and their alignment score were determined.

• MDAR checklist

Data availability

Raw data supporting this study can be found at the Harvard Dataverse https://doi.org/10.7910/DVN/PZ6LRK.

The following dataset was generated:

Author(s)	Year	Dataset title	Dataset URL	Database and Identifier
Nguyen A, Zhao H, Myagmarsuren D, Srinivasan S, Wu D, Chen J, Piszczek G, Schuck P	2024	Replication Data for: Modulation of Biophysical Properties of Nucleocapsid Protein in the Mutant Spectrum of SARS-CoV-2	https://doi.org/10.7910/DVN/PZ6LRK	Harvard Dataverse, 10.7910/DVN/PZ6LRK

References

Abyzov A, Blackledge M, Zweckstetter M. 2022. Conformational dynamics of intrinsically disordered proteins regulate biomolecular condensate chemistry. *Chemical Reviews* **122**:6719–6748. DOI: https://doi.org/10.1021/acs.chemrev.1c00774, PMID: 35179885

Adly AN, Bi M, Carlson CR, Syed AM, Ciling A, Doudna JA, Cheng Y, Morgan DO. 2023. Assembly of SARS-CoV-2 ribonucleosomes by truncated N* variant of the nucleocapsid protein. *The Journal of Biological Chemistry* **299**:105362. DOI: https://doi.org/10.1016/j.jbc.2023.105362, PMID: 37863261

Alderson TR, Pritišanac I, Kolarić Đ, Moses AM, Forman-Kay JD. 2023. Systematic identification of conditionally folded intrinsically disordered regions by AlphaFold2. *PNAS* **120**:2022. DOI: https://doi.org/10.1073/pnas.2304302120

Altschul SF, Madden TL, Schäffer AA, Zhang J, Zhang Z, Miller W, Lipman DJ. 1997. Gapped BLAST and PSI-BLAST: a new generation of protein database search programs. *Nucleic Acids Research* **25**:3389–3402. DOI: https://doi.org/10.1093/nar/25.17.3389

Artesi M, Bontems S, Göbbels P, Franckh M, Maes P, Boreux R, Meex C, Melin P, Hayette MP, Bours V, Durkin K. 2020. A recurrent mutation at position 26340 of SARS-CoV-2 is associated with failure of the E gene quantitative reverse transcription-PCR utilized in a commercial dual-target diagnostic assay. *Journal of Clinical Microbiology* **58**:1–8. DOI: https://doi.org/10.1128/JCM.01598-20, PMID: 32690547

Arzt M, Deschamps J, Schmied C, Pietzsch T, Schmidt D, Tomancak P, Haase R, Jug F. 2022. LABKIT: labeling and segmentation Toolkit for big image data. *Frontiers in Computer Science* **4**:777728. DOI: https://doi.org/10.3389/fcomp.2022.777728

Bershtein S, Serohijos AW, Shakhnovich EI. 2017. Bridging the physical scales in evolutionary biology: from protein sequence space to fitness of organisms and populations. *Current Opinion in Structural Biology* **42**:31–40. DOI: https://doi.org/10.1016/j.sbi.2016.10.013, PMID: 27810574

Bessa LM, Guseva S, Camacho-Zarco AR, Salvi N, Maurin D, Perez LM, Botova M, Malki A, Nanao M, Jensen MR, Ruigrok RWH, Blackledge M. 2022. The intrinsically disordered SARS-CoV-2 nucleoprotein in dynamic complex with its viral partner nsp3a. *Science Advances* **8**:eabm4034. DOI: https://doi.org/10.1126/sciadv.abm4034, PMID: 35044811

Biswal M, Lu J, Song J. 2022. SARS-CoV-2 nucleocapsid protein targets a conserved surface groove of the NTF2-like Domain of G3BP1. *Journal of Molecular Biology* **434**:167516. DOI: https://doi.org/10.1016/j.jmb.2022.167516, PMID: 35240128

Bloom JD, Labthavikul ST, Otey CR, Arnold FH. 2006. Protein stability promotes evolvability. *PNAS* **103**:5869–5874. DOI: https://doi.org/10.1073/pnas.0510098103, PMID: 16581913

Bloom JD, Beichman AC, Neher RA, Harris K. 2023. Evolution of the SARS-CoV-2 mutational spectrum. *Molecular Biology and Evolution* **40**:2022. DOI: https://doi.org/10.1093/molbev/msad085, PMID: 37039557

Bloom JD, Neher RA. 2023. Fitness effects of mutations to SARS-CoV-2 proteins. *Virus Evolution* **9**:vead055. DOI: https://doi.org/10.1093/ve/vead055, PMID: 37727875

Botova M, Camacho-Zarco AR, Tognetti J, Bessa LM, Guseva S, Mikkola E, Salvi N, Maurin D, Herrmann T, Blackledge M. 2024. A Specific Phosphorylation-Dependent Conformational Switch of SARS-CoV-2 Nucleoprotein Inhibits RNA Binding. *bioRxiv*. DOI: https://doi.org/10.1101/2024.02.22.579423

Brocca S, Grandori R, Longhi S, Uversky V. 2020. Liquid-liquid phase separation by intrinsically disordered protein regions of viruses: roles in viral life cycle and control of virus-host interactions. *International Journal of Molecular Sciences* **21**:1–31. DOI: https://doi.org/10.3390/ijms21239045, PMID: 33260713

Brown CJ, Johnson AK, Daughdrill GW. 2010. Comparing models of evolution for ordered and disordered proteins. *Molecular Biology and Evolution* **27**:609–621. DOI: https://doi.org/10.1093/molbev/msp277, PMID: 19923193

Brown CJ, Johnson AK, Dunker AK, Daughdrill GW. 2011. Evolution and disorder. *Current Opinion in Structural Biology* **21**:441–446. DOI: https://doi.org/10.1016/j.sbi.2011.02.005, PMID: 21482101

Carlson CR, Asfaha JB, Ghent CM, Howard CJ, Hartooni N, Safari M, Frankel AD, Morgan DO. 2020. Phosphoregulation of phase separation by the SARS-CoV-2 N protein suggests a biophysical basis for its dual functions. *Molecular Cell* **80**:1092–1103.. DOI: https://doi.org/10.1016/j.molcel.2020.11.025, PMID: 33248025

Carlson CR, Adly AN, Bi M, Howard CJ, Frost A, Cheng Y, Morgan DO. 2022. Reconstitution of the SARS-CoV-2 ribonucleosome provides insights into genomic RNA packaging and regulation by phosphorylation. *The Journal of Biological Chemistry* **298**:102560. DOI: https://doi.org/10.1016/j.jbc.2022.102560, PMID: 36202211

Cascarina SM, Ross ED. 2022. Phase separation by the SARS-CoV-2 nucleocapsid protein: Consensus and open questions. *The Journal of Biological Chemistry* **298**:101677. DOI: https://doi.org/10.1016/j.jbc.2022.101677, PMID: 35131265

Charon J, Barra A, Walter J, Millot P, Hébrard E, Moury B, Michon T. 2018. First experimental assessment of protein intrinsic disorder involvement in an RNA virus natural adaptive process. *Molecular Biology and Evolution* **35**:38–49. DOI: https://doi.org/10.1093/molbev/msx249, PMID: 29029259

Chen K, Xiao F, Hu D, Ge W, Tian M, Wang W, Pan P, Wu K, Wu J. 2020. SARS-CoV-2 nucleocapsid protein interacts with RIG-I and represses RIG-mediated IFN-β production. *Viruses* **13**:47. DOI: https://doi.org/10.3390/v13010047, PMID: 33396605

Chin AF, Zheng Y, Hilser VJ. 2022. Phylogenetic convergence of phase separation and mitotic function in the disordered protein BuGZ. *Protein Science* **31**:822–834. DOI: https://doi.org/10.1002/pro.4270, PMID: 34984754

Cubuk J, Alston JJ, Incicco JJ, Singh S, Stuchell-Brereton MD, Ward MD, Zimmerman MI, Vithani N, Griffith D, Wagoner JA, Bowman GR, Hall KB, Soranno A, Holehouse AS. 2021. The SARS-CoV-2 nucleocapsid protein is dynamic, disordered, and phase separates with RNA. *Nature Communications* **12**:1936. DOI: https://doi.org/10.1038/s41467-021-21953-3, PMID: 33782395

Cubuk J, Alston JJ, Incicco JJ, Holehouse AS, Hall KB, Stuchell-Brereton MD, Soranno A. 2023. The Disordered N-Terminal Tail of SARS CoV-2 Nucleocapsid Protein Forms a Dynamic Complex with RNA. *bioRxiv*. DOI: https://doi.org/10.1101/2023.02.10.527914

Dadonaite B, Crawford KHD, Radford CE, Farrell AG, Yu TC, Hannon WW, Zhou P, Andrabi R, Burton DR, Liu L, Ho DD, Chu HY, Neher RA, Bloom JD. 2023. A pseudovirus system enables deep mutational scanning of the full SARS-CoV-2 spike. *Cell* **186**:1263–1278.. DOI: https://doi.org/10.1016/j.cell.2023.02.001, PMID: 36868218

Davey NE, Travé G, Gibson TJ. 2011. How viruses hijack cell regulation. *Trends in Biochemical Sciences* **36**:159–169. DOI: https://doi.org/10.1016/j.tibs.2010.10.002, PMID: 21146412

Davey NE, Cyert MS, Moses AM. 2015. Short linear motifs - Ex nihilo evolution of protein regulation Short linear motifs - The unexplored frontier of the eukaryotic proteome. *Cell Communication and Signaling: CCS* **13**:9–11. DOI: https://doi.org/10.1186/s12964-015-0120-z

Del Veliz S, Rivera L, Bustos DM, Uhart M. 2021. Analysis of SARS-CoV-2 nucleocapsid phosphoprotein N variations in the binding site to human 14-3-3 proteins. *Biochemical and Biophysical Research Communications* **569**:154–160. DOI: https://doi.org/10.1016/j.bbrc.2021.06.100, PMID: 34246830

de Silva TI, Liu G, Lindsey BB, Dong D, Moore SC, Hsu NS, Shah D, Wellington D, Mentzer AJ, Angyal A, Brown R, Parker MD, Ying Z, Yao X, Turtle L, Dunachie S, Maini MK, Ogg G, Knight JC, Peng Y, et al. 2021. The impact of viral mutations on recognition by SARS-CoV-2 specific T cells. *iScience* **24**:103353. DOI: https://doi.org/10.1016/j.isci.2021.103353, PMID: 34729465

Dinesh DC, Chalupska D, Silhan J, Koutna E, Nencka R, Veverka V, Boura E. 2020. Structural basis of RNA recognition by the SARS-CoV-2 nucleocapsid phosphoprotein. *PLOS Pathogens* **16**:e1009100. DOI: https://doi.org/10.1371/journal.ppat.1009100, PMID: 33264373

Dolan PT, Taguwa S, Rangel MA, Acevedo A, Hagai T, Andino R, Frydman J. 2021. Principles of dengue virus evolvability derived from genotype-fitness maps in human and mosquito cells. *eLife* **10**:e61921. DOI: https://doi.org/10.7554/eLife.61921, PMID: 33491648

Domingo E, Holland JJ. 1997. RNA virus mutations and fitness for survival. *Annual review of microbiology* **51**:151–178. DOI: https://doi.org/10.1146/annurev.micro.51.1.151, PMID: 9343347

Echave J, Wilke CO. 2017. Biophysical models of protein evolution: understanding the patterns of evolutionary sequence divergence. *Annual Review of Biophysics* **46**:85–103. DOI: https://doi.org/10.1146/annurev-biophys-070816-033819, PMID: 28301766

Eftink MR. 2000. Intrinsic fluorescence of proteins. Lakowicz JR (Ed). *Topics in Fluorescence Spectroscopy*. Kluwer Academic Publishers. p. 1–13. DOI: https://doi.org/10.1007/0-306-47102-7_11

Eigen M. 1996. On the nature of virus quasispecies. *Trends in Microbiology* **4**:216–218. DOI: https://doi.org/10.1016/0966-842X(96)20011-3, PMID: 8795155

Eisenberg D, McLachlan AD. 1986. Solvation energy in protein folding and binding. *Nature* **319**:199–203. DOI: https://doi.org/10.1038/319199a0

Elbe S, Buckland-Merrett G. 2017. Data, disease and diplomacy: GISAID's innovative contribution to global health. *Global Challenges* **1**:33–46. DOI: https://doi.org/10.1002/gch2.1018, PMID: 31565258

Finkel Y, Mizrahi O, Nachshon A, Weingarten-Gabbay S, Morgenstern D, Yahalom-Ronen Y, Tamir H, Achdout H, Stein D, Israeli O, Beth-Din A, Melamed S, Weiss S, Israely T, Paran N, Schwartz M, Stern-Ginossar N. 2021. The coding capacity of SARS-CoV-2. *Nature* **589**:125–130. DOI: https://doi.org/10.1038/s41586-020-2739-1, PMID: 32906143

Forsythe HM, Rodriguez Galvan J, Yu Z, Pinckney S, Reardon P, Cooley RB, Zhu P, Rolland AD, Prell JS, Barbar E. 2021. Multivalent binding of the partially disordered SARS-CoV-2 nucleocapsid phosphoprotein dimer to RNA. *Biophysical Journal* **120**:2890–2901. DOI: https://doi.org/10.1016/j.bpj.2021.03.023, PMID: 33794152

Fung TS, Liu DX. 2018. Post-translational modifications of coronavirus proteins: roles and function. *Future Virology* **13**:405–430. DOI: https://doi.org/10.2217/fvl-2018-0008, PMID: 32201497

Garcia-Viloca M, Gao J, Karplus M, Truhlar DG. 2004. How enzymes work: analysis by modern rate theory and computer simulations. *Science* **303**:186–195. DOI: https://doi.org/10.1126/science.1088172, PMID: 14716003

Gerstein M, Chothia C. 1996. Packing at the protein-water interface. *PNAS* **93**:10167–10172. DOI: https://doi.org/10.1073/pnas.93.19.10167, PMID: 8816770

Ghirlando R, Balbo A, Piszczek G, Brown PH, Lewis MS, Brautigam CA, Schuck P, Zhao H. 2013. Improving the thermal, radial, and temporal accuracy of the analytical ultracentrifuge through external references. *Analytical Biochemistry* **440**:81–95. DOI: https://doi.org/10.1016/j.ab.2013.05.011

Gitlin I, Carbeck JD, Whitesides GM. 2006. Why are proteins charged? networks of charge–charge interactions in proteins measured by charge ladders and capillary electrophoresis. *Angewandte Chemie International Edition* **45**:3022–3060. DOI: https://doi.org/10.1002/anie.200502530

Gitlin L, Hagai T, LaBarbera A, Solovey M, Andino R. 2014. Rapid evolution of virus sequences in intrinsically disordered protein regions. *PLOS Pathogens* **10**:e1004529. DOI: https://doi.org/10.1371/journal.ppat.1004529, PMID: 25502394

Gordon DE, Jang GM, Bouhaddou M, Xu J, Obernier K, White KM, O'Meara MJ, Rezelj VV, Guo JZ, Swaney DL, Tummino TA, Hüttenhain R, Kaake RM, Richards AL, Tutuncuoglu B, Foussard H, Batra J, Haas K, Modak M, Kim M, et al. 2020. A SARS-CoV-2 protein interaction map reveals targets for drug repurposing. *Nature* **583**:459–468. DOI: https://doi.org/10.1038/s41586-020-2286-9, PMID: 32353859

Greaney AJ, Starr TN, Bloom JD. 2022. An antibody-escape estimator for mutations to the SARS-CoV-2 receptor-binding domain. *Virus Evolution* **8**:veac021. DOI: https://doi.org/10.1093/ve/veac021, PMID: 35573973

Gupta NT, Vander Heiden JA, Uduman M, Gadala-Maria D, Yaari G, Kleinstein SH. 2015. Change-O: A toolkit for analyzing large-scale B cell immunoglobulin repertoire sequencing data. *Bioinformatics* **31**:3356–3358. DOI: https://doi.org/10.1093/bioinformatics/btv359

Hadfield J, Megill C, Bell SM, Huddleston J, Potter B, Callender C, Sagulenko P, Bedford T, Neher RA. 2018. Nextstrain: real-time tracking of pathogen evolution. *Bioinformatics* **34**:4121–4123. DOI: https://doi.org/10.1093/bioinformatics/bty407

Hagai T, Azia A, Babu MM, Andino R. 2014. Use of host-like peptide motifs in viral proteins is a prevalent strategy in host-virus interactions. *Cell Reports* **7**:1729–1739. DOI: https://doi.org/10.1016/j.celrep.2014.04.052, PMID: 24882001

Ho WL, Huang JR. 2022. The return of the rings: Evolutionary convergence of aromatic residues in the intrinsically disordered regions of RNA-binding proteins for liquid–liquid phase separation. *Protein Science* **31**:1–7. DOI: https://doi.org/10.1002/pro.4317

Hu Y, Lewandowski EM, Tan H, Zhang X, Morgan RT, Zhang X, Jacobs LMC, Butler SG, Gongora MV, Choy J, Deng X, Chen Y, Wang J. 2023. Naturally occurring mutations of SARS-CoV-2 main protease confer drug resistance to nirmatrelvir. *ACS Central Science* **9**:1658–1669. DOI: https://doi.org/10.1021/acscentsci.3c00538, PMID: 37637734

Iserman C, Roden CA, Boerneke MA, Sealfon RSG, McLaughlin GA, Jungreis I, Fritch EJ, Hou YJ, Ekena J, Weidmann CA, Theesfeld CL, Kellis M, Troyanskaya OG, Baric RS, Sheahan TP, Weeks KM, Gladfelter AS. 2020. Genomic RNA elements drive phase separation of the SARS-CoV-2 nucleocapsid. *Molecular Cell* **80**:1078–1091.. DOI: https://doi.org/10.1016/j.molcel.2020.11.041, PMID: 33290746

Jack A, Ferro LS, Trnka MJ, Wehri E, Nadgir A, Nguyenla X, Fox D, Costa K, Stanley S, Schaletzky J, Yildiz A. 2021. SARS-CoV-2 nucleocapsid protein forms condensates with viral genomic RNA. *PLOS Biology* **19**:e3001425. DOI: https://doi.org/10.1371/journal.pbio.3001425, PMID: 34634033

Javed I, Butt MA, Khalid S, Shehryar T, Amin R, Syed AM, Sadiq M. 2023. Face mask detection and social distance monitoring system for COVID-19 pandemic. *Multimedia Tools and Applications* **82**:14135–14152. DOI: https://doi.org/10.1007/s11042-022-13913-w, PMID: 36196269

Johnson BA, Zhou Y, Lokugamage KG, Vu MN, Bopp N, Crocquet-Valdes PA, Kalveram B, Schindewolf C, Liu Y, Scharton D, Plante JA, Xie X, Aguilar P, Weaver SC, Shi PY, Walker DH, Routh AL, Plante KS, Menachery VD. 2022. Nucleocapsid mutations in SARS-CoV-2 augment replication and pathogenesis. *PLOS Pathogens* **18**:e1010627. DOI: https://doi.org/10.1371/journal.ppat.1010627, PMID: 35728038

Kar M, Dar F, Welsh TJ, Vogel LT, Kühnemuth R, Majumdar A, Krainer G, Franzmann TM, Alberti S, Seidel CAM, Knowles TPJ, Hyman AA, Pappu RV. 2022. Phase-separating RNA-binding proteins form heterogeneous distributions of clusters in subsaturated solutions. *PNAS* **119**:e2202222119. DOI: https://doi.org/10.1073/pnas.2202222119, PMID: 35787038

Kauzmann W. 1959. Some factors in the interpretation of protein denaturationadvances in protein chemistry. *Advance in Protein Chemistry* **14**:1–63. DOI: https://doi.org/10.1016/S0065-3233(08)60608-7

Kepler L, Hamins-Puertolas M, Rasmussen DA. 2021. Decomposing the sources of SARS-CoV-2 fitness variation in the United States. *Virus Evolution* **7**:veab073. DOI: https://doi.org/10.1093/ve/veab073, PMID: 34642604

Klein S, Cortese M, Winter SL, Wachsmuth-Melm M, Neufeldt CJ, Cerikan B, Stanifer ML, Boulant S, Bartenschlager R, Chlanda P. 2020. SARS-CoV-2 structure and replication characterized by in situ cryo-electron tomography. *Nature Communications* **11**:5885. DOI: https://doi.org/10.1038/s41467-020-19619-7

Kruse T, Benz C, Garvanska DH, Lindqvist R, Mihalic F, Coscia F, Inturi R, Sayadi A, Simonetti L, Nilsson E, Ali M, Kliche J, Moliner Morro A, Mund A, Andersson E, McInerney G, Mann M, Jemth P, Davey NE, Överby AK, et al. 2021. Large scale discovery of coronavirus-host factor protein interaction motifs reveals SARS-CoV-2 specific mechanisms and vulnerabilities. *Nature Communications* **12**:1–13. DOI: https://doi.org/10.1038/s41467-021-26498-z

Kubinski HC, Despres HW, Johnson BA, Schmidt MM, Jaffrani SA, Mills MG, Lokugamage K, Dumas CM, Shirley DJ, Estes LK, Pekosz A, Crothers JW, Roychoudhury P, Greninger AL, Jerome KR, Di Genova BM, Walker DH, Ballif BA, Ladinsky MS, Bjorkman PJ, et al. 2024. Variant Mutation in SARS-CoV-2 Nucleocapsid Enhances Viral Infection via Altered Genomic Encapsidation. *bioRxiv*. DOI: https://doi.org/10.1101/2024.03.08.584120

Kuo L, Hurst-Hess KR, Koetzner CA, Masters PS. 2016. Analyses of coronavirus assembly interactions with interspecies membrane and nucleocapsid protein chimeras. *Journal of Virology* **90**:4357–4368. DOI: https://doi.org/10.1128/JVI.03212-15, PMID: 26889024

Lafforgue G, Michon T, Charon J. 2022. Analysis of the contribution of intrinsic disorder in shaping potyvirus genetic Diversity. *Viruses* **14**:1959. DOI: https://doi.org/10.3390/v14091959, PMID: 36146764

Lässig M, Mustonen V, Walczak AM. 2017. Predicting evolution. *Nature Ecology & Evolution* **1**:77. DOI: https://doi.org/10.1038/s41559-017-0077, PMID: 28812721

Leary S, Gaudieri S, Parker MD, Chopra A, James I, Pakala S, Alves E, John M, Lindsey BB, Keeley AJ, Rowland-Jones SL, Swanson MS, Ostrov DA, Bubenik JL, Das SR, Sidney J, Sette A, COVID-19 Genomics UK (COG-UK) consortium, de Silva TI, Phillips E, et al. 2021. Generation of a novel SARS-CoV-2 Sub-genomic RNA due to the R203K/G204R variant in nucleocapsid: homologous recombination has potential to change SARS-CoV-2 at both protein and RNA level. *Pathogens & Immunity* **6**:27–49. DOI: https://doi.org/10.20411/pai.v6i2.460, PMID: 34541432

Li JY, Liao CH, Wang Q, Tan YJ, Luo R, Qiu Y, Ge XY. 2020. The ORF6, ORF8 and nucleocapsid proteins of SARS-CoV-2 inhibit type I interferon signaling pathway. *Virus Research* **286**:198074. DOI: https://doi.org/10.1016/j.virusres.2020.198074, PMID: 32589897

Liberles DA, Teichmann SA, Bahar I, Bastolla U, Bloom J, Bornberg-Bauer E, Colwell LJ, de Koning APJ, Dokholyan NV, Echave J, Elofsson A, Gerloff DL, Goldstein RA, Grahnen JA, Holder MT, Lakner C, Lartillot N, Lovell SC, Naylor G, Perica T, et al. 2012. The interface of protein structure, protein biophysics, and molecular evolution. *Protein Science* **21**:769–785. DOI: https://doi.org/10.1002/pro.2071, PMID: 22528593

Lin Y, Currie SL, Rosen MK. 2017. Intrinsically disordered sequences enable modulation of protein phase separation through distributed tyrosine motifs. *The Journal of Biological Chemistry* **292**:19110–19120. DOI: https://doi.org/10.1074/jbc.M117.800466, PMID: 28924037

López-Muñoz AD, Kosik I, Holly J, Yewdell JW. 2022. Cell surface SARS-CoV-2 nucleocapsid protein modulates innate and adaptive immunity. *Science Advances* **8**:eabp9770. DOI: https://doi.org/10.1126/sciadv.abp9770, PMID: 35921414

Lu S, Ye Q, Singh D, Cao Y, Diedrich JK, Yates JR, Villa E, Cleveland DW, Corbett KD. 2021. The SARS-CoV-2 nucleocapsid phosphoprotein forms mutually exclusive condensates with RNA and the membrane-associated M protein. *Nature Communications* **12**:502. DOI: https://doi.org/10.1038/s41467-020-20768-y, PMID: 33479198

Ma J, Zhao H, Sandmaier J, Alexander Liddle J, Schuck P. 2016. Variable field analytical ultracentrifugation: II gravitational sweep sedimentation velocity. *Biophysical Journal* **110**:103–112. DOI: https://doi.org/10.1016/j.bpj.2015.11.027, PMID: 26745414

Mao AH, Crick SL, Vitalis A, Chicoine CL, Pappu RV. 2010. Net charge per residue modulates conformational ensembles of intrinsically disordered proteins. *PNAS* **107**:8183–8188. DOI: https://doi.org/10.1073/pnas.0911107107

Masters PS. 2019. Coronavirus genomic RNA packaging. *Virology* **537**:198–207. DOI: https://doi.org/10.1016/j.virol.2019.08.031, PMID: 31505321

Mears HV, Young GR, Sanderson T, Harvey R, Crawford M, Snell DM, Fowler AS, Hussain S, Nicod J, Peacock TP, Emmott E, Finsterbusch K, Luptak J, Wall E, Williams B, Gandhi S, Swanton C, Bauer DL. 2022. Emergence of new subgenomic mRNAs in SARS-CoV-2. *bioRxiv*. DOI: https://doi.org/10.1101/2022.04.20.488895

Mihalič F, Simonetti L, Giudice G, Sander MR, Lindqvist R, Peters MBA, Benz C, Kassa E, Badgujar D, Inturi R, Ali M, Krystkowiak I, Sayadi A, Andersson E, Aronsson H, Söderberg O, Dobritzsch D, Petsalaki E, Överby AK, Jemth P, et al. 2023. Large-scale phage-based screening reveals extensive pan-viral mimicry of host short linear motifs. *Nature Communications* **14**:2409. DOI: https://doi.org/10.1038/s41467-023-38015-5

Mirdita M, Schütze K, Moriwaki Y, Heo L, Ovchinnikov S, Steinegger M. 2022. ColabFold: making protein folding accessible to all. *Nature Methods* **19**:679–682. DOI: https://doi.org/10.1038/s41592-022-01488-1, PMID: 35637307

Moses D, Ginell GM, Holehouse AS, Sukenik S. 2023. Intrinsically disordered regions are poised to act as sensors of cellular chemistry. *Trends in Biochemical Sciences* **48**:1019–1034. DOI: https://doi.org/10.1016/j.tibs.2023.08.001

Obermeyer F, Jankowiak M, Barkas N, Schaffner SF, Pyle JD, Yurkovetskiy L, Bosso M, Park DJ, Babadi M, MacInnis BL, Luban J, Sabeti PC, Lemieux JE. 2022. Analysis of 6.4 million SARS-CoV-2 genomes identifies mutations associated with fitness. *Science* **376**:1327–1332. DOI: https://doi.org/10.1126/science.abm1208, PMID: 35608456

Osorio D, Rondón-Villarreal P, Torres R. 2015. Peptides: a package for data mining of antimicrobial peptides. *The R Journal* **7**:4. DOI: https://doi.org/10.32614/RJ-2015-001

Oulas A, Zanti M, Tomazou M, Zachariou M, Minadakis G, Bourdakou MM, Pavlidis P, Spyrou GM. 2021. Generalized linear models provide a measure of virulence for specific mutations in SARS-CoV-2 strains. *PLOS ONE* **16**:e0238665. DOI: https://doi.org/10.1371/journal.pone.0238665, PMID: 33497392

Pan P, Shen M, Yu Z, Ge W, Chen K, Tian M, Xiao F, Wang Z, Wang J, Jia Y, Wang W, Wan P, Zhang J, Chen W, Lei Z, Chen X, Luo Z, Zhang Q, Xu M, Li G, et al. 2021. SARS-CoV-2 N protein promotes NLRP3 inflammasome activation to induce hyperinflammation. *Nature Communications* **12**:1–17. DOI: https://doi.org/10.1038/s41467-021-25015-6

Papadopoulos JS, Agarwala R. 2007. COBALT: constraint-based alignment tool for multiple protein sequences. *Bioinformatics* **23**:1073–1079. DOI: https://doi.org/10.1093/bioinformatics/btm076

Pappu RV, Cohen SR, Dar F, Farag M, Kar M. 2023. Phase transitions of associative biomacromolecules. *Chemical Reviews* **123**:8945–8987. DOI: https://doi.org/10.1021/acs.chemrev.2c00814

Perdikari TM, Murthy AC, Ryan VH, Watters S, Naik MT, Fawzi NL. 2020. SARS-CoV-2 nucleocapsid protein phase-separates with RNA and with human hnRNPs. *The EMBO Journal* **39**:1–35. DOI: https://doi.org/10.15252/embj.2020106478

Pettersen EF, Goddard TD, Huang CC, Meng EC, Couch GS, Croll TI, Morris JH, Ferrin TE. 2021. UCSF ChimeraX: Structure visualization for researchers, educators, and developers. *Protein Science* **30**:70–82. DOI: https://doi.org/10.1002/pro.3943, PMID: 32881101

Pontoriero L, Schiavina M, Korn SM, Schlundt A, Pierattelli R, Felli IC. 2022. NMR reveals specific tracts within the intrinsically disordered regions of the SARS-CoV-2 nucleocapsid protein involved in RNA encountering. *Biomolecules* **12**:929. DOI: https://doi.org/10.3390/biom12070929, PMID: 35883485

Redzic JS, Lee E, Born A, Issaian A, Henen MA, Nichols PJ, Blue A, Hansen KC, D'Alessandro A, Vögeli B, Eisenmesser EZ. 2021. The inherent dynamics and interaction sites of the SARS-CoV-2 nucleocapsid N-terminal region. *Journal of Molecular Biology* **433**:167108. DOI: https://doi.org/10.1016/j.jmb.2021.167108, PMID: 34161778

Riback JA, Katanski CD, Kear-Scott JL, Pilipenko EV, Rojek AE, Sosnick TR, Drummond DA. 2017. Stress-triggered phase separation is an adaptive, evolutionarily tuned response. *Cell* **168**:1028–1040.. DOI: https://doi.org/10.1016/j.cell.2017.02.027, PMID: 28283059

Ribeiro-Filho HV, Jara GE, Batista FAH, Schleder GR, Costa Tonoli CC, Soprano AS, Guimarães SL, Borges AC, Cassago A, Bajgelman MC, Marques RE, Trivella DBB, Franchini KG, Figueira ACM, Benedetti CE, Lopes-de-Oliveira PS. 2022. Structural dynamics of SARS-CoV-2 nucleocapsid protein induced by RNA binding. *PLOS Computational Biology* **18**:e1010121. DOI: https://doi.org/10.1371/journal.pcbi.1010121, PMID: 35551296

Rochman ND, Wolf YI, Faure G, Mutz P, Zhang F, Koonin EV. 2021. Ongoing global and regional adaptive evolution of SARS-CoV-2. *PNAS* **118**:1–10. DOI: https://doi.org/10.1073/pnas.2104241118, PMID: 34292871

Roden CA, Dai Y, Giannetti CA, Seim I, Lee M, Sealfon R, McLaughlin GA, Boerneke MA, Iserman C, Wey SA, Ekena JL, Troyanskaya OG, Weeks KM, You L, Chilkoti A, Gladfelter AS. 2022. Double-stranded RNA drives SARS-CoV-2 nucleocapsid protein to undergo phase separation at specific temperatures. *Nucleic Acids Research* **50**:8168–8192. DOI: https://doi.org/10.1093/nar/gkac596, PMID: 35871289

Różycki B, Boura E. 2022. Conformational ensemble of the full-length SARS-CoV-2 nucleocapsid (N) protein based on molecular simulations and SAXS data. *Biophysical Chemistry* **288**:106843. DOI: https://doi.org/10.1016/j.bpc.2022.106843, PMID: 35696898

Saldivar-Espinoza B, Macip G, Pujadas G, Garcia-Vallve S. 2022. Could nucleocapsid be a next-generation COVID-19 vaccine candidate? *International Journal of Infectious Diseases* **125**:231–232. DOI: https://doi.org/10.1016/j.ijid.2022.11.002, PMID: 36347459

Saldivar-Espinoza B, Garcia-Segura P, Novau-Ferré N, Macip G, Martínez R, Puigbò P, Cereto-Massagué A, Pujadas G, Garcia-Vallve S. 2023. The mutational landscape of SARS-CoV-2. *International Journal of Molecular Sciences* **24**:9072. DOI: https://doi.org/10.3390/ijms24109072, PMID: 37240420

Savastano A, Ibáñez de Opakua A, Rankovic M, Zweckstetter M. 2020. Nucleocapsid protein of SARS-CoV-2 phase separates into RNA-rich polymerase-containing condensates. *Nature Communications* **11**:6041. DOI: https://doi.org/10.1038/s41467-020-19843-1, PMID: 33247108

Schmidt U, Weigert M, Broaddus C, Myers G. 2018. Cell detection with star-convex Polygons in. Frangi A, Schnabel J, Davatzikos C, Alberola-López C, Fichtinger G (Eds). *Medical image computing and computer assisted intervention – MICCAI 2018, Lecture Notes in computer science*. Springer. p. 265–273. DOI: https://doi.org/10.1007/978-3-030-00934-2_30

Schuck P, Zhao H, Brautigam CA, Ghirlando R. 2015. *Basic principles of analytical ultracentrifugation*. CRC Press. DOI: https://doi.org/10.1201/b19028

Schuck P. 2016. *Sedimentation Velocity Analytical Ultracentrifugation: Discrete Species and Size-Distributions of Macromolecules and Particles*. CRC Press. DOI: https://doi.org/10.1201/9781315367231

Schuck P, Zhao H. 2017. *Sedimentation velocity analytical ultracentrifugation: interacting systems*. CRC Press. DOI: https://doi.org/10.1201/b21988

Schuck P, Zhao H. 2023. Diversity of short linear interaction motifs in SARS-CoV-2 nucleocapsid protein. *mBio* **14**:e0238823. DOI: https://doi.org/10.1128/mbio.02388-23, PMID: 38018991

Serohijos AWR, Shakhnovich EI. 2014. Merging molecular mechanism and evolution: theory and computation at the interface of biophysics and evolutionary population genetics. *Current Opinion in Structural Biology* **26**:84–91. DOI: https://doi.org/10.1016/j.sbi.2014.05.005, PMID: 24952216

Shuler G, Hagai T. 2022. Rapidly evolving viral motifs mostly target biophysically constrained binding pockets of host proteins. *Cell Reports* **40**:111212. DOI: https://doi.org/10.1016/j.celrep.2022.111212, PMID: 35977510

Sikosek T, Chan HS. 2014. Biophysics of protein evolution and evolutionary protein biophysics. *Journal of the Royal Society, Interface* **11**:20140419. DOI: https://doi.org/10.1098/rsif.2014.0419, PMID: 25165599

Starr TN, Thornton JW. 2016. Epistasis in protein evolution. *Protein Science* **25**:1204–1218. DOI: https://doi.org/10.1002/pro.2897, PMID: 26833806

Stevens LJ, Pruijssers AJ, Lee HW, Gordon CJ, Tchesnokov EP, Gribble J, George AS, Hughes TM, Lu X, Li J, Perry JK, Porter DP, Cihlar T, Sheahan TP, Baric RS, Götte M, Denison MR. 2022. Mutations in the SARS-CoV-2 RNA-dependent RNA polymerase confer resistance to remdesivir by distinct mechanisms. *Science Translational Medicine* **14**:eabo0718. DOI: https://doi.org/10.1126/scitranslmed.abo0718, PMID: 35482820

Syed AM, Taha TY, Tabata T, Chen IP, Ciling A, Khalid MM, Sreekumar B, Chen PY, Hayashi JM, Soczek KM, Ott M, Doudna JA. 2021. Rapid assessment of SARS-CoV-2-evolved variants using virus-like particles. *Science* **374**:1626–1632. DOI: https://doi.org/10.1126/science.abl6184, PMID: 34735219

Syed AM, Ciling A, Khalid MM, Sreekumar B, Chen PY, Kumar GR, Silva I, Milbes B, Kojima N, Hess V, Shacreaw M, Lopez L, Brobeck M, Turner F, Spraggon L, Taha TY, Tabata T, Chen IP, Ott M, Doudna JA. 2022. Omicron mutations enhance infectivity and reduce antibody neutralization of SARS-CoV-2 virus-like particles. *bioRxiv*. DOI: https://doi.org/10.1101/2021.12.20.21268048

Tarczewska A, Kolonko-Adamska M, Zarębski M, Dobrucki J, Ożyhar A, Greb-Markiewicz B. 2021. The method utilized to purify the SARS-CoV-2 N protein can affect its molecular properties. *International Journal of Biological Macromolecules* **188**:391–403. DOI: https://doi.org/10.1016/j.ijbiomac.2021.08.026, PMID: 34371045

Tian Y, Zhang G, Liu H, Ding P, Jia R, Zhou J, Chen Y, Qi Y, Du J, Liang C, Zhu X, Wang A. 2022. Screening and identification of B cell epitope of the nucleocapsid protein in SARS-CoV-2 using the monoclonal antibodies. *Applied Microbiology and Biotechnology* **106**:1151–1164. DOI: https://doi.org/10.1007/s00253-022-11769-6, PMID: 35037999

Tokuriki N, Oldfield CJ, Uversky VN, Berezovsky IN, Tawfik DS. 2009. Do viral proteins possess unique biophysical features? *Trends in Biochemical Sciences* **34**:53–59. DOI: https://doi.org/10.1016/j.tibs.2008.10.009, PMID: 19062293

Tokuriki N, Tawfik DS. 2009. Protein dynamism and evolvability. *Science* **324**:203–207. DOI: https://doi.org/10.1126/science.1169375, PMID: 19359577

Viana R, Moyo S, Amoako DG, Tegally H, Scheepers C, Althaus CL, Anyaneji UJ, Bester PA, Boni MF, Chand M, Choga WT, Colquhoun R, Davids M, Deforche K, Doolabh D, du Plessis L, Engelbrecht S, Everatt J, Giandhari J, Giovanetti M, et al. 2022. Rapid epidemic expansion of the SARS-CoV-2 Omicron variant in southern Africa. *Nature* **603**:679–686. DOI: https://doi.org/10.1038/s41586-022-04411-y

Wang K, Yu S, Ji X, Lakner C, Griffing A, Thorne JL. 2015. Roles of solvent accessibility and gene expression in modeling protein sequence evolution. *Evolutionary Bioinformatics Online* **11**:85–96. DOI: https://doi.org/10.4137/EBO.S22911, PMID: 25987828

Wang Y, Lei R, Nourmohammad A, Wu NC. 2021. Antigenic evolution of human influenza H3N2 neuraminidase is constrained by charge balancing. *eLife* **10**:e72516. DOI: https://doi.org/10.7554/eLife.72516, PMID: 34878407

Wu F, Zhao S, Yu B, Chen YM, Wang W, Song ZG, Hu Y, Tao ZW, Tian JH, Pei YY, Yuan ML, Zhang YL, Dai FH, Liu Y, Wang QM, Zheng JJ, Xu L, Holmes EC, Zhang YZ. 2020. A new coronavirus associated with human respiratory disease in China. *Nature* **579**:265–269. DOI: https://doi.org/10.1038/s41586-020-2008-3

Wu W, Cheng Y, Zhou H, Sun C, Zhang S. 2023. The SARS-CoV-2 nucleocapsid protein: its role in the viral life cycle, structure and functions, and use as a potential target in the development of vaccines and diagnostics. *Virology Journal* **20**:6. DOI: https://doi.org/10.1186/s12985-023-01968-6

Yao H, Song Y, Chen Y, Wu N, Xu J, Sun C, Zhang J, Weng T, Zhang Z, Wu Z, Cheng L, Shi D, Lu X, Lei J, Crispin M, Shi Y, Li L, Li S. 2020. Molecular architecture of the SARS-CoV-2 virus. *Cell* **183**:730–738.. DOI: https://doi.org/10.1016/j.cell.2020.09.018

Yaron TM, Heaton BE, Levy TM, Johnson JL, Jordan TX, Cohen BM, Kerelsky A, Lin T-Y, Liberatore KM, Bulaon DK, Van Nest SJ, Koundouros N, Kastenhuber ER, Mercadante MN, Shobana-Ganesh K, He L, Schwartz RE, Chen S, Weinstein H, Elemento O, et al. 2022. Host protein kinases required for SARS-CoV-2 nucleocapsid phosphorylation and viral replication. *Science Signaling* **15**:1–17. DOI: https://doi.org/10.1126/scisignal.abm0808, PMID: 36282911

Yu H, Guan F, Miller H, Lei J, Liu C. 2023. The role of SARS-CoV-2 nucleocapsid protein in antiviral immunity and vaccine development. *Emerging Microbes & Infections* **12**:2164219. DOI: https://doi.org/10.1080/22221751.2022.2164219

Zarin T, Tsai CN, Nguyen Ba AN, Moses AM. 2017. Selection maintains signaling function of a highly diverged intrinsically disordered region. *PNAS* **114**:E1450–E1459. DOI: https://doi.org/10.1073/pnas.1614787114, PMID: 28167781

Zarin T, Strome B, Peng G, Pritišanac I, Forman-Kay JD, Moses AM. 2021. Identifying molecular features that are associated with biological function of intrinsically disordered protein regions. *eLife* **10**:e60220. DOI: https://doi.org/10.7554/eLife.60220, PMID: 33616531

Zhang X, Zheng R, Li Z, Ma J. 2023. Liquid-liquid phase separation in viral function. *Journal of Molecular Biology* **435**:167955. DOI: https://doi.org/10.1016/j.jmb.2023.167955, PMID: 36642156

Zhao H, Ghirlando R, Alfonso C, Arisaka F, Attali I, Bain DL, Bakhtina MM, Becker DF, Bedwell GJ, Bekdemir A, Besong TMD, Birck C, Brautigam CA, Brennerman W, Byron O, Bzowska A, Chaires JB, Chaton CT, Cölfen H, Connaghan KD, et al. 2015. A multilaboratory comparison of calibration accuracy and the performance of external references in analytical ultracentrifugation. *PLOS ONE* **10**:e0126420. DOI: https://doi.org/10.1371/journal.pone.0126420

Zhao H, Wu D, Nguyen A, Li Y, Adão RC, Valkov E, Patterson GH, Piszczek G, Schuck P. 2021. Energetic and structural features of SARS-CoV-2 N-protein co-assemblies with nucleic acids. *iScience* **24**:102523. DOI: https://doi.org/10.1016/j.isci.2021.102523

Zhao H, Nguyen A, Wu D, Li Y, Hassan SA, Chen J, Shroff H, Piszczek G, Schuck P. 2022. Plasticity in structure and assembly of SARS-CoV-2 nucleocapsid protein. *PNAS Nexus* **1**:pgac049. DOI: https://doi.org/10.1093/pnasnexus/pgac049, PMID: 35783502

Zhao H, Wu D, Hassan SA, Nguyen A, Chen J, Piszczek G, Schuck P. 2023. A conserved oligomerization domain in the disordered linker of coronavirus nucleocapsid proteins. *Science Advances* **9**:eadg6473. DOI: https://doi.org/10.1126/sciadv.adg6473, PMID: 37018390

Zhao H, Syed AM, Khalid MM, Nguyen A, Ciling A, Wu D, Yau WM, Srinivasan S, Esposito D, Doudna JA, Piszczek G, Ott M, Schuck P. 2024. Assembly of SARS-CoV-2 nucleocapsid protein with nucleic acid. *Nucleic Acids Research* **52**:6647–6661. DOI: https://doi.org/10.1093/nar/gkae256, PMID: 38587193